

REMARKS

In the Final Office Action dated 29 December 2005, claims 1-16 were pending; claims 1-11 and 13-16 were rejected; and claim 12 was objected to but considered to include patentable subject matter.

By way of this Amendment, claim 16 is amended to better represent the present invention. No new matter was added by way of this amendment.

In the office action claims 1, 3-11, 13-14, and 16 were rejected under 35 USC § 103 (a) as being unpatentable over Trampert in view of Zhu. Further, claims 1, 3-8, 10, 13-14, and 16 were rejected under 35 USC § 103 (a) as being unpatentable over Trampert in view of Silawongsawat.

The present claim 1 includes “estimating a P-SV propagator from said recorded seismic wavefield”. It is submitted that this step goes beyond the mere knowledge of a matrix representation of the P-SV propagator. This step requires an estimation of the P-SV propagator from the recorded seismic wavefield.

In the following paragraphs, it will be shown that neither Trampert nor Zhu nor Silawongsawat teach a way of estimating a P-SV propagator from a recorded seismic wavefield.

Regarding first Trampert, Trampert makes an explicit statement that the method presented is only applicable to the SH propagator matrix. With regard to the method used by Trampert, it is stated that “the spectral ratio of the total surface record over borehole record gives a measurement of the propagator” (see Trampert, p. 291, 2nd col, 2nd paragraph). The approach of Trampert is only valid for SH waves as such wave types do not undergo conversion at the surface.

Regarding secondly Zhu, it has to be noted that Zhu is not concerned with an estimate of the P-SV propagator. Zhu takes the Thompson-Haskell expression of the P-SV propagator

(equation 20). The Thompson-Haskell expression of the P-SV propagator is equivalent to the expression given by Aki and others. Zhu shows that the P-SV converges to a static solution if the frequencies go to zero. Zhu shows further that static deformation from earthquakes can be derived using the P-SV propagator. However, the important point is that Zhu does not show how to estimate the S-PV propagator from a recorded seismic wavefield. Instead, Zhu uses a predefined earth model referred to as "PREM" (see page 5, 2nd col, bottom paragraph) to define the parameters of the P-SV propagator.

When finally considering Silawongsawat, it is again clear that as far as the formulation of the P-SV propagator is concerned, Silawongsawat recites the known expressions based on Backus, Thompson-Haskell, Aki and others. For the present discussion, it should be noted that Silawongsawat, similar to Zhu, teaches methods for numerical simulation. In these methods, the P-SV propagator is not estimated from recorded seismic data, but derived solely from the parameters which define the earth model used in the simulation.

In the rejection of claims 1, 3-11, 13-14, and 16 over Trampert in view of Zhu or in view of Silawongsawat, the Examiner neglected an important feature of independent claims 1 and 16. More specifically, the Examiner appears to equate the prior knowledge of an mathematical expression for the P-SV propagator with the estimation of a P-SV propagator from recorded seismic data. It is, however, evident that knowledge of the P-SV propagator is not equal to a method of estimating it from real data. The Applicants have not denied that mathematical expressions of the P-SV operator are prior knowledge. In fact equations (9) – (14) of the specification represent such an expression. Those equations are taken from Aki et al. and serve as a starting point for the estimation of the P-SV operator from recorded data.

In this context, Applicants would like to comment that being restricted to claim 12, which was deemed to include allowable subject matter, is too narrow. The equations (17)-(21) denote only an intermediate step in the estimation of the P-SV operator. Once the terms of the P-SV propagator is split in real and imaginary parts (as per equation (17) – (21)), it can be quickly realized that, for example, for near vertical incidents of the waves, the main components of the propagator can be approximately estimated from the recorded horizontal and vertical waves only. This variant of the present invention is explained in the last

paragraph of page 19 of the specification. The amended claim 16 broadens the scope of claim 12 to include all the methods described on page 19.

Therefore, Applicants respectfully traverse all of the section 103 rejections in the Office Action because the cited references do not teach or suggest all of the claim limitations of independent claims 1 and 16. Specifically, the Examiner has not shown a reference that describes estimating a P-SV propagator from recorded seismic data.

Moreover, Applicants respectfully submit that the Trampert, Zhu and Silawongsawat references do not contain any suggestion or motivation for combining the references. Whilst Trampert relates to identifying parameters relating to near-surface layers Zhu and Silawongsawat, both relate to modelling. As such, it would require impermissible hindsight to combine the references.

Further, it appears worth noting that since the January 15, 2003 GB filing date of the present application, two papers by the co-inventors on the method of the present invention have been published in peer-reviewed journals. This underlines the fact that the scientific community has accepted the present invention as representing novel and original work. The publications are

1. R. van Vossen, A. Curtis and J. Trampert 2005. Subsonic near-surface P velocity and low S velocity observations using propagator inversion. *Geophysics*, 70(4), pages R15-R23; and

2. R. van Vossen, J. Trampert and A. Curtis 2004. Propagator and wave-equation inversion for near-receiver material properties. *Geophys. J. Int.*, 157, 796-812.

Courtesy copies of these documents are provided herewith.

Hence, it is respectfully requested that the section 103 rejections of independent claims 1 and claim 16 be withdrawn. Additionally, it is respectfully requested

that the section 103 rejection of all claims depending from independent claims 1 and 16 also be withdrawn.

In light of the above remarks, Applicants believe that the present application and claims 1-16 as amended are in proper condition for allowance. Such allowance is earnestly requested. If the Examiner is contemplating any action other than allowance of all pending claims, the Examiner is urged to contact Applicant's representative, Jody Lynn DeStefanis, at (203) 431-5505.

Applicants believe that no fee is due in connection with this response. However, in the event that a fee or refund is determined to be due, the Commissioner is hereby authorized to charge any underpayment or credit any overpayment to Deposit Account No 19-0615.

Respectfully submitted,


Jody Lynn DeStefanis
Registration No. 44,653

Schlumberger Doll Research Center
36 Old Quarry Road
Ridgefield, CT 06877-4108
Phone: (203) 431-5505
Fax: (203) 431-5640

Subsonic near-surface P-velocity and low S-velocity observations using propagator inversion

Robbert van Vossen¹, Andrew Curtis², and Jeannot Trampert¹

ABSTRACT

Detailed knowledge of near-surface P- and S-wave velocities is important for processing and interpreting multicomponent land seismic data because (1) the entire wavefield passes through and is influenced by the near-surface soil conditions, (2) both source repeatability and receiver coupling also depend on these conditions, and (3) near-surface P- and S-wave velocities are required for wavefield decomposition and demultiple methods. However, it is often difficult to measure these velocities with conventional techniques because sensitivity to shallow-wave velocities is low and because of the presence of sharp velocity contrasts or gradients close to the earth's free surface. We demonstrate that these near-surface P- and S-wave velocities can be obtained using a propagator inversion. This approach requires data recorded by at least one multicomponent geophone at the surface and an additional multicomponent geophone at depth. The propagator between them then contains all information on the

medium parameters governing wave propagation between the geophones at the surface and at depth. Hence, inverting the propagator gives local estimates for these parameters. This technique has been applied to data acquired in Zeist, the Netherlands. The near-surface sediments at this site are unconsolidated sands with a thin vegetation soil on top, and the sediments considered are located above the groundwater table. A buried geophone was positioned 1.05 m beneath receivers on the surface. Propagator inversion yielded low near-surface velocities, namely, 270 ± 15 m/s for the compressional-wave velocity, which is well below the sound velocity in air, and 150 ± 9 m/s for the shear velocity. Existing methods designed for imaging deeper structures cannot resolve these shallow material properties. Furthermore, velocities usually increase rapidly with depth close to the earth's surface because of increasing confining pressure. We suspect that for this reason, subsonic near-surface P-wave velocities are not commonly observed.

INTRODUCTION

Strong near-surface velocity contrasts are often encountered in land seismic surveys. Both P- and S-wave velocities may increase by nearly an order of magnitude at the interface defining the top of the bedrock, and P-velocities increase up to 100% across the top depth of total water saturation (Stümpel et al., 1984; Goforth and Hayward, 1992).

Detailed knowledge of near-surface velocities is essential for engineering applications and groundwater and environmental projects (Ward, 1990). Furthermore, this knowledge is required to correctly process and interpret (multicomponent) land data. For instance, near-surface soil conditions have a significant influence on source wavelet and radiation patterns (Kähler and Meissner, 1983; Aritman, 2001). Also, wavefield

decomposition, which enables independent interpretation of up- and downgoing P- and S-waves, requires the free-surface reflectivity to be known accurately (e.g., Dankbaar, 1985; Wapenaar et al., 1990; Robertsson and Curtis, 2002). Wavefield decomposition is a prerequisite for demultiple methods (Verschuur et al., 1992), which are especially important in media with a near-surface low-velocity layer that may act as a wave guide in which energy may propagate over long distances with little loss from geometric spreading. This could mask reflections from a deeper target (Hunter et al., 1984; Robertsson et al., 1996). Demultiple methods remove these guided waves.

While shallow material properties are especially important for processing and interpretation of multicomponent seismic data, near-surface wave velocities usually cannot be resolved

Presented at the 73rd International Meeting, SEG, 2003. Manuscript received by the Editor October 21, 2003; revised manuscript received December 17, 2004; published online July 7, 2005.

¹Utrecht University, Department of Earth Sciences, Budapestlaan 4, 3584 CD Utrecht, the Netherlands. E-mail: vossen@geo.uu.nl; trampert@geo.uu.nl.

²Schlumberger Cambridge Research, High Cross, Madingley Road, Cambridge CB3 0EL, United Kingdom; and The University of Edinburgh, School of GeoSciences, Grant Institute, West Mains Road, Edinburgh, EH9 3JW, Scotland. E-mail: curtis@cambridge.oilfield.slb.com.

© 2005 Society of Exploration Geophysicists. All rights reserved.

with an acquisition geometry designed for imaging deeper structure. Detailed information can, however, be obtained with shallow, high-resolution reflection and refraction experiments (Doornenbal and Helbig, 1983; Hunter et al., 1984; Steeples and Miller, 1990). These techniques use arrays of closely spaced geophones and high frequencies to obtain detailed images of the shallow subsurface.

Subsonic P-wave velocities have been observed with these shallow, high-resolution seismic experiments by analyzing moveout velocities close to the source (Birkelo et al., 1987; Bachrach and Nur, 1998; Bachrach et al., 1998; Baker et al., 1999), whereas they are not commonly observed using conventional seismic techniques. This is a consequence of the different depth sensitivities of these methods, combined with a near-surface velocity gradient caused by increasing confining pressure. A drawback of estimating near-source moveout velocities is that the complexity of the near-source field requires careful processing and interpretation of these types of data to avoid misinterpretation of recorded events (Michaels, 2002).

Recently, Curtis and Robertsson (2002) introduced a technique for estimating local near-surface velocities using a 3D geophone configuration. Geophones are not only deployed at the surface but also at shallow depths to enhance imaging of the near-surface without having to perform an additional high-resolution experiment. With the proposed 3D geophone configuration, spatial wavefield derivatives can be approximated, allowing inversion of the wave equation for near-surface P- and S-wave velocities (Curtis and Robertsson, 2002). An advantage of this method is its applicability to the complete wavefield; a drawback is its sensitivity to deployment-related errors (Muijs et al., 2002).

We present results from a technique referred to as propagator inversion (PI) (Trampert et al., 1993; Van Vossen et al., 2004). This technique also uses a 3D geophone configuration to determine near-surface P- and S-wave velocities, but it avoids explicit computation of spatial wavefield derivatives and is therefore less sensitive to deployment-related errors. Moreover, it does not require measurement and interpretation of moveout velocities in the near-source region, and it can be incorporated in a seismic survey for imaging deeper structure without having to perform an additional high-resolution experiment.

PROPAGATOR ESTIMATION FROM DATA

Propagator matrices were introduced in seismology by Thomson (1950) and Haskell (1953) and generalized by Gilbert and Backus (1965). These matrices describe the propagation of plane waves through a horizontally layered medium. Throughout this paper, the free surface is used as a reference level. The propagator can then be interpreted as a wavefield-extrapolation filter. Application of the propagator to the recorded wavefield at the free surface gives the wavefield at depth Δz .

Trampert et al. (1993) introduced SH PI to obtain the SH-wave velocity structure and the quality factor in a borehole. This propagator can be obtained from the recorded data by taking the spectral ratio of a downhole record over a surface record. It is completely determined by the medium parameters governing wavefield propagation between these two records. Recently, Van Vossen et al. (2004) formulated propagator estimation for the elastic P-SV case. We briefly review this con-

cept before we discuss the inversion scheme for near-surface material parameters.

In an isotropic medium, the propagator naturally decomposes into SH and coupled P-SV waves. The anelastic SH case is fully treated by Trampert et al. (1993). We only review the elastic P-SV case here. Denote the inline particle-velocity component by v_1 and the vertical component by v_3 . The full propagator is a 4×4 matrix, and the boundary conditions state that the free surface is stress free, so that the wavefield at depth Δz is related to the wavefield recorded at the free surface ($z = 0$) by:

$$\begin{pmatrix} v_1(\omega, x, \Delta z) \\ v_3(\omega, x, \Delta z) \end{pmatrix} = \begin{pmatrix} P_{11} & P_{13} \\ P_{31} & P_{33} \end{pmatrix} \begin{pmatrix} v_1(\omega, x, 0) \\ v_3(\omega, x, 0) \end{pmatrix}. \quad (1)$$

For an elastic, homogeneous medium, with P velocity α and S velocity β , the propagator coefficients read in the time domain (Aki and Richards, 2002; Van Vossen et al., 2004) as

$$P_{11} = \beta^2 p^2 G_1^P + [(1 - 2\beta^2 p^2)/2] G_1^S, \quad (2)$$

$$P_{33} = [(1 - 2\beta^2 p^2)/2] G_1^P + \beta^2 p^2 G_1^S, \quad (3)$$

$$P_{13} = [p(1 - 2\beta^2 p^2)/(2q_P)] G_2^P - \beta^2 p q_S G_2^S, \quad (4)$$

$$P_{31} = \beta^2 p q_P G_2^P - [p(1 - 2\beta^2 p^2)/(2q_S)] G_2^S, \quad (5)$$

where

$$G_1^P = \delta(t + q_P \Delta z) + \delta(t - q_P \Delta z), \quad (6)$$

$$G_2^P = \delta(t + q_P \Delta z) - \delta(t - q_P \Delta z), \quad (7)$$

$$G_1^S = \delta(t + q_S \Delta z) + \delta(t - q_S \Delta z), \quad (8)$$

$$G_2^S = \delta(t + q_S \Delta z) - \delta(t - q_S \Delta z). \quad (9)$$

The horizontal slowness is denoted by p , and the vertical slownesses q_P and q_S are

$$q_P = (\alpha^{-2} - p^2)^{1/2}, \quad (10)$$

$$q_S = (\beta^{-2} - p^2)^{1/2}. \quad (11)$$

These theoretical expressions show that P_{11} and P_{33} are symmetric around $t = 0$, whereas P_{13} and P_{31} are antisymmetric around $t = 0$. Thus, in the frequency domain, P_{11} and P_{33} are entirely real, and P_{13} and P_{31} are purely imaginary. As a result, we can directly estimate the components of $P_{ij}(\omega)$ by equating real and imaginary parts in equation 1. In the following, we denote the propagator coefficients estimated from the data with $\hat{P}(\omega)$. The explicit expressions for estimating $\hat{P}(\omega)$ are

$$\begin{aligned} \hat{P}_{11} &= \{\Re[v_3(\omega, 0)]\Re[v_1(\omega, \Delta z)] \\ &\quad + \Im[v_3(\omega, 0)]\Im[v_1(\omega, \Delta z)]\}/D(\omega), \end{aligned} \quad (12)$$

$$\begin{aligned} \hat{P}_{33} &= \{\Re[v_1(\omega, 0)]\Re[v_3(\omega, \Delta z)] \\ &\quad + \Im[v_1(\omega, 0)]\Im[v_3(\omega, \Delta z)]\}/D(\omega), \end{aligned} \quad (13)$$

$$\begin{aligned} \hat{P}_{13} &= i\{\Re[v_1(\omega, 0)]\Im[v_1(\omega, \Delta z)] \\ &\quad - \Im[v_1(\omega, 0)]\Re[v_1(\omega, \Delta z)]\}/D(\omega), \end{aligned} \quad (14)$$

$$\begin{aligned} \hat{P}_{31} &= i\{\Re[v_3(\omega, 0)]\Im[v_3(\omega, \Delta z)] \\ &\quad - \Im[v_3(\omega, 0)]\Re[v_3(\omega, \Delta z)]\}/D(\omega), \end{aligned} \quad (15)$$

with the denominator $D(\omega)$ given by

$$D(\omega) = \Re[v_3(\omega, 0)]\Re[v_1(\omega, 0)] + \Im[v_3(\omega, 0)]\Im[v_1(\omega, 0)]. \quad (16)$$

In these equations, $\Re[v_1(\omega, \Delta z)]$ is the real part of $v_1(\omega, \Delta z)$, $\Im[v_1(\omega, \Delta z)]$ is the imaginary part, and i denotes the imaginary unit $\sqrt{-1}$. Note that the symmetry properties used to obtain explicit expressions for the propagator filters break down in the viscoelastic case. Then, only the SH propagator can be directly obtained from the data (Trampert et al., 1993).

Van Vossen et al. (2004) computed $\tilde{\mathbf{P}}$ with a stabilized spectral division using the so-called water-level method (Helmberger and Wiggins, 1971). Stabilization is required because of a limited bandwidth of $D(\omega)$, and interfering waves may introduce internal notches in $D(\omega)$. However, a problem associated with this method is that the amount of stabilization can influence the estimates for the propagator (Ammon, 1991), which may affect the inversion results as well (Van Vossen et al., 2004). To avoid these problems, we decided instead to implement the spectral divisions in the time domain using a Wiener deconvolution scheme. Either symmetric (\tilde{P}_{11} and \tilde{P}_{33}) or antisymmetric filters (\tilde{P}_{13} and \tilde{P}_{31}) around $t = 0$ are constructed with N independent coefficients. Details on the implementation of the acausal Wiener deconvolution can be found in Appendix A.

PROPAGATOR INVERSION (PI)

In the previous section, we showed that $\tilde{\mathbf{P}}$ can be obtained from data recorded by one surface geophone and one at depth. In this section, we outline the inverse procedure for estimating the near-surface velocities α and β from $\tilde{\mathbf{P}}$.

A flow diagram for the inverse problem is shown in Figure 1. The 3D receiver configuration used for the Zeist field experiment in the Netherlands, conducted to test propagator estimation and inversion, is shown in Figure 2. We discuss this experiment in detail in the next section. The configuration has multicomponent geophones positioned in a cross shape at the surface. Two geophones are buried at the center of the receiving group. Strictly speaking, propagator estimation requires only one multicomponent geophone positioned at the surface and a second geophone at depth. Then, the horizontal slowness also needs to be constrained by the inverse procedure.

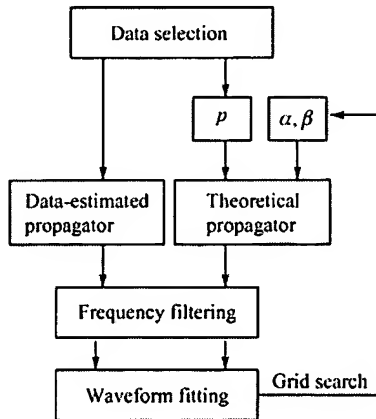


Figure 1. Propagator inversion scheme for α and β .

However, we do not have to incorporate horizontal slowness in the inverse procedure when a short array of geophones is deployed at the surface, since it can be measured directly.

PI consists of the following steps. First, a data window is selected to isolate an arrival. The window is tapered at its edges by a cosine taper. Second, the selected data are used as input for propagator estimation. The horizontal slowness p of the dominant arrival in this time window can be determined using the array of geophones in the inline direction x . This is accomplished by estimating the time shifts for which the stack power is optimized. The remaining unknown parameters in the theoretical propagator for a homogeneous isotropic medium are α and β (equations 2–11). Values for α and β are selected using a grid-search technique. A physical bound is imposed such that $\beta < \alpha/\sqrt{2}$, i.e., the Poisson's ratio has to be positive. Given values for α , β , and p , the theoretical propagator can be evaluated. Before comparing the waveforms of the theoretical propagator \mathbf{P} to the data-estimated propagator $\tilde{\mathbf{P}}$, frequency filtering is necessary since $\tilde{\mathbf{P}}$ is band-limited, whereas \mathbf{P} has an infinite bandwidth. After bandwidth equalization, the propagator waveforms can be compared to each other. The L2 norm was used as the objective function:

$$E_{ij} = \left\{ \sum_{t=-N\Delta t}^{N\Delta t} [\tilde{P}_{ij}(t) - P_{ij}(t, \alpha, \beta, p)]^2 \right\}^{1/2}, \quad (17)$$

with $i, j = 1, 3$. The objective function for the joint inverse of all propagator coefficients is given by the sum of all individual misfit functions,

$$E_{tot} = E_{11} + E_{13} + E_{31} + E_{33}. \quad (18)$$

Estimates for α and β can be obtained by minimizing E_{tot} .

APPLICATION ON ZEIST FIELD DATA

We illustrate PI on a field data set acquired in Zeist, the Netherlands. On this site, the near-surface material mainly consists of unconsolidated sands, with a thin layer of vegetal soil on top.

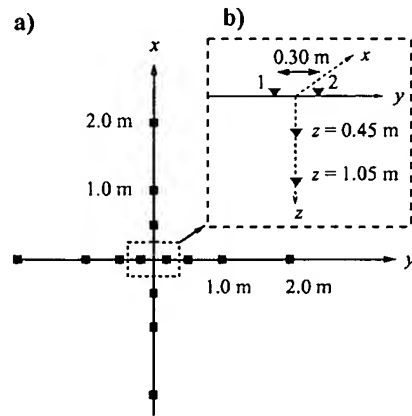


Figure 2. 3D receiver configuration for the Zeist field experiment, (a) top view and (b) front view. All geophones were multicomponent geophones, and the source positions were located on the x -axis.

Data acquisition

A walkaway noise test was performed with 3C 4.5-Hz geophones at offsets between 0.75 and 84 m, with 0.75-m geophone spacing. These data (Figure 3) show that ground roll and guided waves are dominant in the recordings. In addition, measurements were made with a dense 3D 3C receiving configuration that will be used for PI (see Figure 2). Geophones were positioned in a cross shape at the surface. In the x -direction, receivers were located at 0.50, 1.00, and 2.00 m distance to the center of the configuration; in the y -direction, the distances were 0.15, 0.50, 1.00, and 2.00 m. The buried geophones were positioned at 0.45 and 1.05 m depth, respectively. Geophones can be buried efficiently in unconsolidated sediments using a hand ground drill. This approach minimizes

the medium perturbations caused by burial of geophones. For the dense 3D 3C group, data were acquired using 11 different source positions located between 35- and 85-m offset. The shot spacing was 5.0 m, and all shot points were located on the x -axis. The experiment was repeated four times for every shot position. During the whole experiment, a weight drop was used; a steel ball of about 37 kg was dropped from approximately 3.5 m height on a steel plate resting on the ground. The recording instrument was a Bison Spectra with 48 channels, and the time-sampling interval was 0.25 ms.

Data selection and estimation of horizontal slowness

In theory, the propagator method is valid for a single slowness, i.e., isolating an arrival as uncontaminated as possible by other arrivals. On the other hand, considering only very short time windows results in a poor signal-to-noise ratio. Synthetic experiments demonstrate that PI is insensitive to small slowness variations in the selected data (Van Vossen et al., 2004). Therefore, we selected data windows including all events arriving before the ground roll. For each shot position, time windows that contain the selected data are listed in Table 1. A cosine taper with 0.01 s length was applied to both edges of the window. An example of data selected for slowness estimation is shown in Figure 4. A bandpass filter with cut-off frequencies between 40 and 140 Hz was applied to these recordings. The events shown may be interpreted as trapped waves above the groundwater table. Because there are significant differences in the recorded amplitudes on the inline component, we decided to estimate p using only the vertical component of the recorded particle velocity. These slowness estimates are given for each shot position in Table 1. The differences between the estimated horizontal slownesses for the different source positions are small.

Propagator estimation and inversion

Contrary to horizontal-slowness estimation, no frequency filtering was applied to the selected data prior to propagator estimation. An example of the data used for propagator estimation is shown in Figure 5. It shows that recordings rapidly change with depth, especially on the vertical component. At 0.45 m depth, high frequencies are strongly attenuated compared to the recordings obtained at the free surface and at 1.05 m depth. On the other hand, the low-frequency content of the signal decays with depth. This characteristic behavior is caused by interference between the free-surface incident wave and its reflected and converted waves.

Interpretation of the data recorded on the horizontal component is difficult. The two surface geophones show significant amplitude differences in the high-frequency part of the spectrum. For lower frequencies, on the other hand, there is excellent agreement between these recordings. This observation could indicate coupling differences between these two surface geophones (Krohn, 1984). Another interesting observation is that the amount of energy recorded in the 50- to 60-Hz frequency band is small, although we did not apply a notch filter to the data.

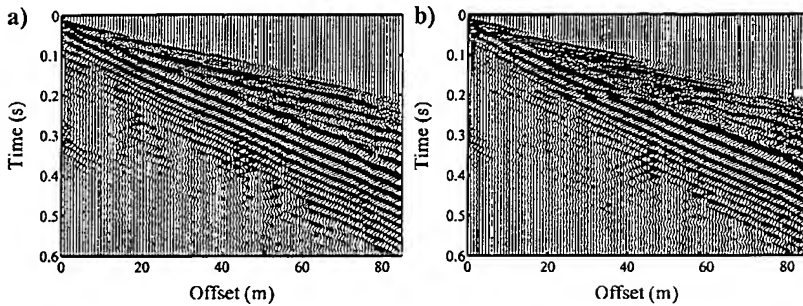


Figure 3. Walkaway noise survey for (a) v_x and (b) v_z . The panels are displayed with trace normalization.

Table 1. Horizontal slowness estimates for each shot position. Data are selected in time windows with t between t_1 and t_2 .

Shot number	Offset (m)	t_1 (s)	t_2 (s)	p (ms/m)	$\sigma(p)$ (ms/m)
1	85	0.19	0.26	2.10	0.11
2	80	0.18	0.25	2.12	0.07
3	75	0.17	0.24	2.23	0.03
4	70	0.16	0.23	2.18	0.06
5	65	0.15	0.22	2.20	0.06
6	60	0.14	0.21	2.15	0.06
7	55	0.13	0.20	2.12	0.04
8	50	0.11	0.18	2.11	0.03
9	45	0.09	0.17	2.23	0.05
10	40	0.08	0.16	2.19	0.05
11	35	0.07	0.14	2.21	0.03
Mean				2.17	0.05

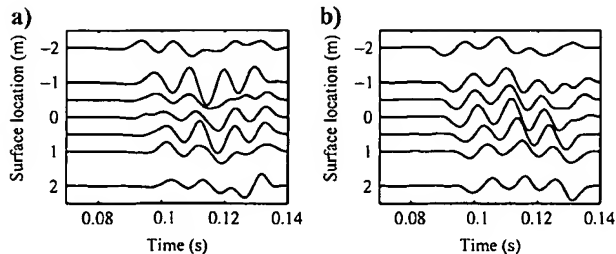


Figure 4. (a) Inline- and (b) vertical-component recordings with the source located at 35 m distance to the center of the receiver group.

We demonstrate PI first using surface geophone 1 and the buried geophone at 1.05 m depth. Then, we consider the data recorded by surface geophone 2. Given the frequency content of the signal and the time-sampling interval of 0.25 ms, accurate velocity estimation with the geophone buried at 0.45 m depth is, in our opinion, not feasible.

Figure 6 shows the data-estimated propagator for each shot position. The frequency passband is between 40 and 140 Hz. The theoretical propagator \mathbf{P} is shown with α and β for which E_{tot} is minimized. There is good agreement between $\hat{\mathbf{P}}$ and \mathbf{P} for most individual shots. Since the changes in the estimated horizontal slowness are small (Table 1), stacking of the data-estimated propagator components over all source positions is not in conflict with the single slowness assumption. This process enhances the signal-to-noise ratio of the data-estimated propagator. Figure 6 shows that an excellent fit is obtained between the averaged propagator components and the best-fitting theoretical propagator.

The constraints offered by each individual propagator component are shown in Figure 7a-d. Misfit functions are shown for the stacked propagator, and the minima of the prestack propagators illustrate the uncertainty. No computations are performed with combinations for α and β for which the Poisson's ratio becomes negative. The misfit functions show that P_{11} and P_{31} are dominantly sensitive to variations in β , whereas P_{33} is more sensitive to variations in α . P_{13} contains information on both α and β . Because P_{33} is dominantly sensitive to variations in α , $(\beta p)^2 \ll 1$ (equation 3). This is confirmed by Table 1. Thus, for near-vertical incident waves, the PI is dominantly sensitive to phase differences rather than amplitude effects as a result of interaction of the incident wavefield with the free surface. However, close to the critical angle for incident S-waves, the amplitude coefficient of P_{13} changes rapidly, which results in sensitivity for both α and β .

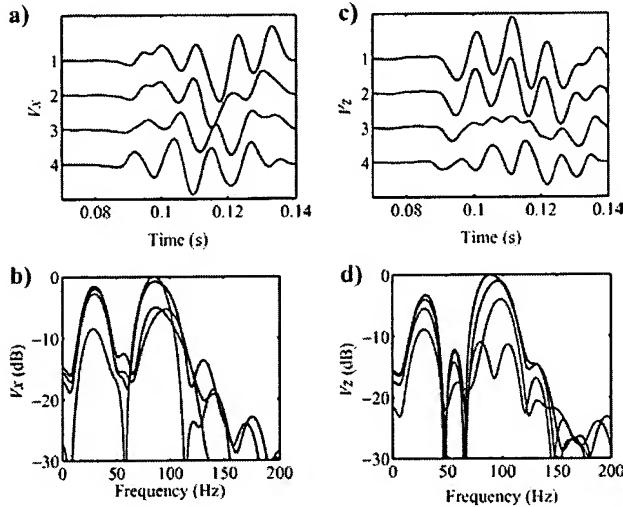


Figure 5. Traces and amplitude spectra for v_x (a, b) and for v_z (c, d) for different depths, recorded at 35-m offset. The black and blue traces are the recordings acquired at the free surface by the geophones labeled 1 and 2 (Figure 2); the red traces were acquired at 0.45 m depth and the green traces at 1.05 m depth.

Figure 7e illustrates the joint inversion for all propagator coefficients. Both α and β are well constrained. The minimum of the joint inversion is equal to the average of all minima of the misfit functions for each individual shot. We obtain the following estimates: $\alpha = 270 \pm 15$ m/s and $\beta = 150 \pm 9$ m/s. The uncertainties given are the standard deviations of the variation of best estimates for the individual shots.

So far we have only discussed the data-estimated propagator obtained using surface geophone 1. Because there are significant differences between the horizontal component recordings 1 and 2 (Figure 5), it is important to assess the consequences of these data differences on propagator estimation and inversion. This allows us to determine whether PI is robust in the presence of realistic data errors. Figure 8 shows that the match between $\hat{\mathbf{P}}$ and \mathbf{P} is not as good compared to the results for surface geophone 1, although the fit is good for the first three shot points and for P_{33} . This propagator coefficient is not significantly affected by data variations on the horizontal component: it relates the vertical component acquired at the free surface to the same component at depth (equation 1). The high-cut frequency was lowered to 100 Hz to reduce the

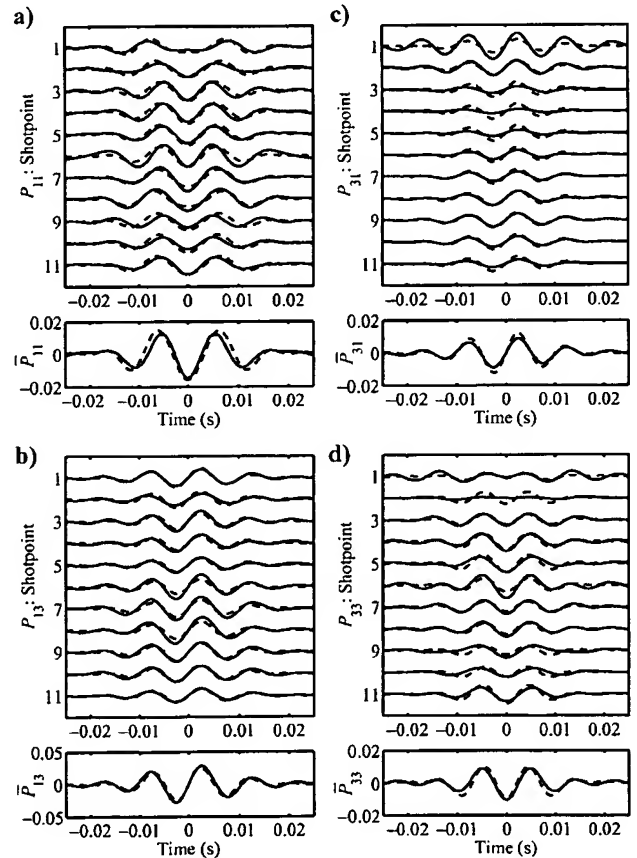


Figure 6. Individual and averaged (stacked) data-estimated propagators (solid) compared to the best fitting theoretical propagator (dashed). Shown are (a) P_{11} , (b) P_{13} , (c) P_{31} , and (d) P_{33} . The data-estimated propagators are computed using surface geophone 1 and the buried geophone at 1.05 m depth. Frequency filters are applied with a passband between 40 and 140 Hz.

effects of coupling errors to the velocity estimation. The misfit function for the joint inverse of all stacked propagators is shown in Figure 7f. The velocities corresponding to the minimum of E_{tot} are $\alpha = 230$ m/s and $\beta = 155$ m/s. Averaging all individual shots gives $\alpha = 244 \pm 20$ m/s and $\beta = 152 \pm 14$ m/s. The estimates for β agree well with the previously obtained velocity estimates, whereas α is less consistent. For shotpoints 1, 2, and 3, which show a good match between $\tilde{\mathbf{P}}$ and \mathbf{P} , we find that $\alpha \geq 260$ m/s.

Although geophones 1 and 2 were close together (0.30 m between them), the horizontal-component data recorded by these two geophones significantly differ for frequencies above 70 Hz. These amplitude differences are attributed to geophone-ground coupling. This refers to the accuracy with which a geophone measures the actual ground motion. It is especially relevant for horizontal-component recordings. A well-coupled horizontal geophone has a coupling-resonance frequency of 130 Hz, whereas poorly coupled horizontal geophones could have significantly lower (down to 30 Hz) resonance frequencies (Krohn 1984). For frequencies much lower than the coupling-resonance frequency, the geophone accurately follows the ground motion.

The results of surface geophone 1 are not sensitive to changes in the high-cut frequency from 100 up to 140 Hz. In-

creasing this frequency reduces the uncertainty in the velocity estimates. For surface geophone 2, on the other hand, increasing this frequency resulted in poor fits of the propagator coefficients and large uncertainties in the estimated velocities. Therefore, we decided to use different frequency bands for the application of PI to data acquired by surface geophones 1 and 2. The obtained results are barely influenced by the choice of the low-cut frequency. Lowering this frequency to 20 Hz yielded similar velocity estimates, although the data misfit between \mathbf{P} and $\tilde{\mathbf{P}}$ increased somewhat, resulting in larger uncertainties attached to these estimates. Therefore, we selected 40 Hz as the low-cut frequency.

Thus, the analysis indicates that best results are obtained with the data recorded by surface geophone 1: inversion results are stable up to 140 Hz, a better data fit is obtained, and the data have a better resolving power for near-surface P- and S-wave velocities. Although the data quality of the recordings of surface geophone 2 is poorer, the estimate for the S-wave velocity is in agreement with the results obtained with surface geophone 1, and the difference between the obtained P-wave velocities is approximately 10% of the estimated value. This

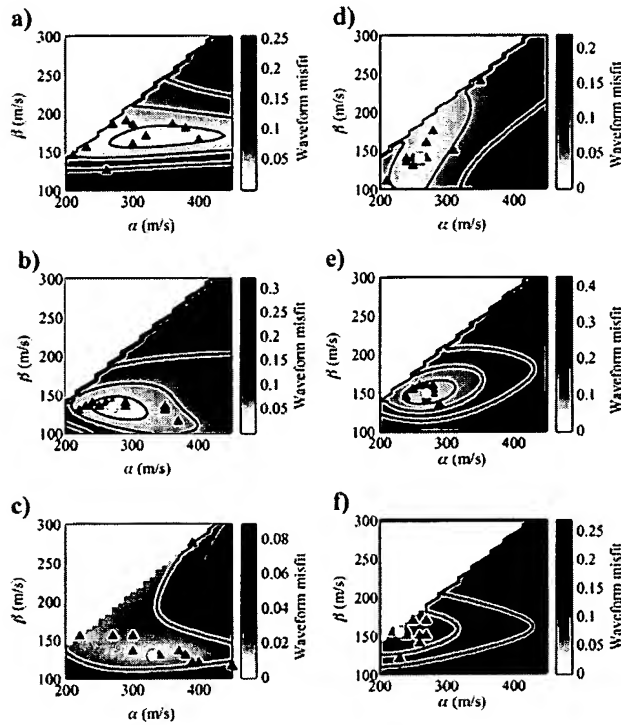


Figure 7. Waveform misfit functions (a) E_{11} , (b) E_{13} , (c) E_{31} , (d) E_{33} for poststack P_{11} , P_{13} , P_{31} , and P_{33} computed using surface geophone 1. The combined constraints are shown in (e). The joint inverse results using surface geophone 2 are shown in (f). Contours are drawn for $E_{ij} = \min(E_{ij}) + c$, with $c = 0.02, 0.05$, and 0.10 , and the indices i and j take the values 1 or 3. The open circle denotes the minimum of E_{ij} , and the triangles indicate the positions of the minima of E_{ij} for each individual shot. No computations are performed in the nonphysical region $\beta > \alpha/\sqrt{2}$.

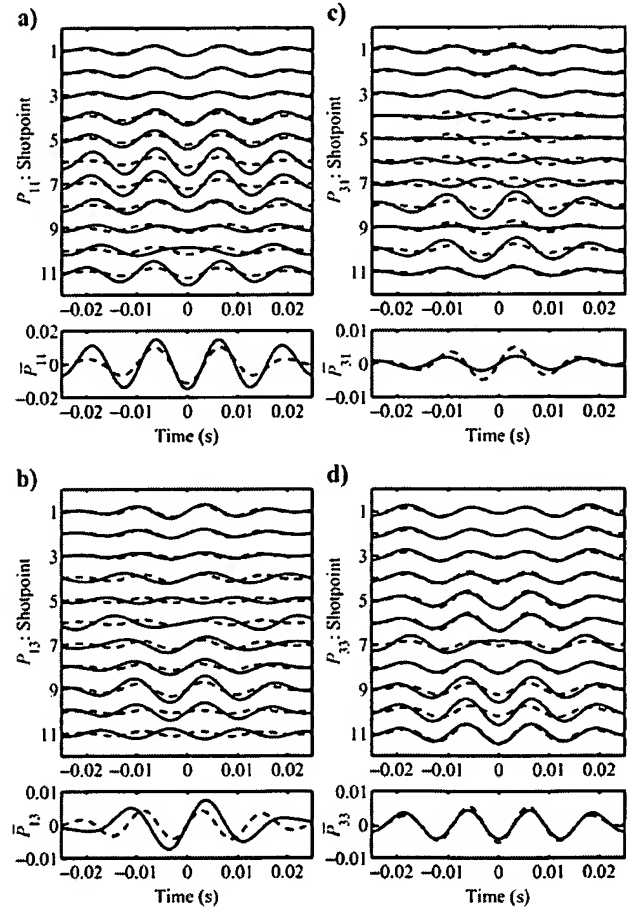


Figure 8. Individual and averaged data-estimated propagators (solid) compared to the best-fitting theoretical propagator (dashed). Shown are (a) P_{11} , (b) P_{13} , (c) P_{31} , and (d) P_{33} . The data-estimated propagators are computed using surface geophone 2 and the buried geophone at 1.05 m depth. Frequency filters are applied with a passband between 40 and 100 Hz.

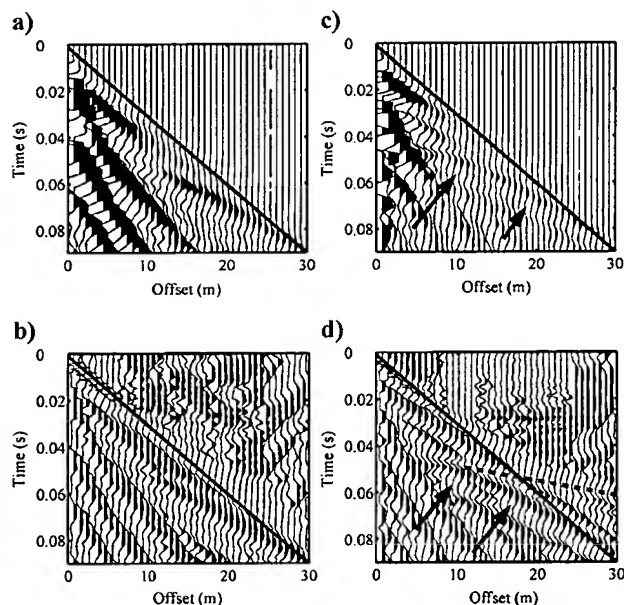


Figure 9. Near-source traces of walkaway noise survey for (a) v_x , (b) v_x with 0.005 s AGC window, (c) v_z , and (d) v_z with 0.005 s AGC window. The airwave is indicated by the solid line, the groundwater refraction by the dashed line, and the arrows indicate the reflected P-wave at the groundwater table.

indicates that the propagator inversion is robust in the presence of measurement errors.

DISCUSSION

Low near-surface velocities are obtained with PI, namely, $\alpha = 270 \pm 15$ m/s and $\beta = 150 \pm 9$ m/s using geophone 1. The Poisson's ratio σ that corresponds to these velocities is 0.28 with an uncertainty range between 0.18 and 0.34. Because the Poisson's ratio is sensitive to perturbations in the estimated velocities, it is difficult to make a sensible lithological interpretation. Despite this uncertainty, we may argue that the observed Poisson's ratio lies between the end-member models for dry, gas-saturated sands with $\sigma \in [0.0 \text{ } 0.22]$ and water-saturated sands with $\sigma \in [0.38 \text{ } 0.50]$ (Bourbié et al., 1987), which qualitatively makes sense because the considered sediment was partially water-saturated.

To test the results of PI, we analyzed the Zeist walkaway noise spread with recordings between 0- and 84-m offset. Near-offset sections of these data are shown in Figure 9. The receiver spacing is 0.75 m. No frequency filtering was applied to these multicomponent recordings. The airwave is clearly visible on both the inline and vertical components in the automatic gain control (AGC) plots. In the offset range between 0 and 10 m, we do not observe coherent energy arriving before the airwave. Events with a higher moveout velocity arrive just after the airwave. This indicates that the near-surface velocity is low, and that velocities increase with depth close to the free surface. Between 15- and 30-m offset, the refracted wave from the water table can be observed, and also the reflected

wave from this interface can easily be identified on the vertical component. Thus, the near-offset section of the walkaway noise spread is qualitatively in agreement with the P-wave velocity obtained with PI for the very shallow near-surface.

In comparison to the results obtained with PI, we found a higher P-wave velocity with a dispersion analysis of guided waves. This difference can be attributed to the different depth sensitivity of dispersion analysis. Propagator inversion is only sensitive to wave velocities between the free surface and the buried geophone, whereas dispersion analysis is sensitive to velocities in the entire layer above the water table. For this reason, these low P- and S-wave velocities are not commonly observed in seismic surveys with a deeper target.

Although shallow material properties may influence the actual wave propagation, we believe that these have most impact on the measured wavefield. Both energy transmitted into the ground and recordings of the wavefield by geophones depend on the near-surface soil conditions. The repeatability of the source mostly depends on the (an)elastic properties of the soil (Aritman, 2001). Both the amount of energy radiated into the ground and the radiation pattern are influenced by the near-source material properties. Lateral variations in near-surface material properties could lead to poor repeatability of the source, degrading the quality of the seismic section. In addition, the measurements of the recording instruments differ from the actual ground motion. The so-called receiver coupling is influenced by the stiffness of the soil (Krohn, 1984). As a consequence, differences between recordings of adjacent receivers can exist as a result of coupling differences. Coupling errors especially affect the quality of converted-wave data. Thus, correct processing and interpretation of seismic data acquired in a land seismic survey require an understanding of both source and receiver coupling effects, and such an understanding may be facilitated by the very near-surface velocity estimates obtained using PI.

Another issue is the interaction of the wavefield with the free surface. Usually, we are only interested in the free-surface incident P- and S-waves, while receivers placed on land measure the interaction of these incident wavefields with the free surface. In principle, we can obtain the free-surface incident P- and S-waves using wavefield decomposition. Wavefield decomposition requires as input the free-surface reflectivity, which depends on the P- and S-wave velocities just below the free surface. Because we measure the wavefield exactly at the free surface, we should not use effective or averaged medium parameters for wavefield decomposition. Thus, the very shallow material properties obtained with PI may improve wavefield decomposition and demultiple methods.

Although application of the propagator method would require additional effort in acquiring data, we demonstrate that the technique provides additional information relevant for a land seismic survey. The propagator method can be incorporated into a seismic survey without having to perform an additional high-resolution experiment.

Finally, it should be mentioned that propagator estimation assumes that the medium is elastic. Although attenuation can be significant in the weathered layer, it does not affect the obtained results, since the dominant wavelength of the analyzed signal is not much smaller than the distance between the surface and the buried geophone.

CONCLUSIONS

The data-estimated propagator contains all information on the material parameters governing wave propagation between the free surface and the depth of a buried geophone. We applied PI on Zeist field data to determine the local near-surface velocities. This inversion yielded subsonic compressional wave velocity, $\alpha = 270 \pm 15$ m/s, and a low shear velocity, $\beta = 150 \pm 9$ m/s for the top meter.

Although very shallow anomalies are considered to have a small impact on the wavefield propagation, these may significantly influence the wavefield recordings. Both the energy transmitted into the subsurface by the source and receiver coupling depend on very shallow material properties. Hence, lateral changes in material properties could lead to poor repeatability of the source and receiver coupling differences. Also, corrections for the interaction of the wavefield with the free surface require these shallow wave velocities to be known.

ACKNOWLEDGMENTS

We thank Schlumberger for financially supporting this work. We further thank Henk van der Meer, Tim van Zon, and Stefan Carpentier for their help acquiring the field data, and Everhard Muyzert, Associate Editor J. Xia, and two anonymous reviewers for their constructive comments.

APPENDIX A

PROPAGATOR ESTIMATION USING WIENER DECONVOLUTION

In this section, we demonstrate the procedure to obtain the propagator filters, which are either symmetric or antisymmetric about $t = 0$, using Wiener deconvolution. We closely follow Yilmaz (2001) in our derivation, with the exception that we estimate acausal filters with symmetry conditions around $t = 0$.

Suppose that $f(t)$ and $g(t)$ are continuous signals, and that $h(t)$ is given by the deconvolution of $f(t)$ by $g(t)$:

$$h(t) = f(t) * g(t)^{-1}, \quad (\text{A-1})$$

or, equivalently,

$$g(t) * h(t) = f(t), \quad (\text{A-2})$$

where $*$ is the convolution operator. The function $h(t)$ represents here the unknown propagator. Crosscorrelating equation A-2 with $g(t)$ gives

$$R(t) * h(t) = q(t), \quad (\text{A-3})$$

where $R(t)$ denotes the autocorrelation of $g(t)$ and

$$q(t) = \int_{-\infty}^{\infty} f(t + \tau)g(\tau)d\tau. \quad (\text{A-4})$$

Assume that we may approximate the propagator $h(t)$ by a filter with $2M + 1$ independent coefficients. This reads, denoting the time series with a vector,

$$\mathbf{h} = [h_{-M} \ h_{-M+1} \ \dots \ h_{-1} \ h_0 \ h_1 \ \dots \ h_{M-1} \ h_M]^T, \quad (\text{A-5})$$

where T is the transpose operator. For a correlation with a maximum correlation length of $N + 1$, \mathbf{q} has $2N + 1$ coefficients, and reads

coefficients, and reads

$$\mathbf{q} = [q_{-N} \ q_{-N+1} \ \dots \ q_{-1} \ q_0 \ q_1 \ \dots \ q_{N-1} \ q_N]^T. \quad (\text{A-6})$$

Then, we may recast equation A-3 in a discrete form:

$$\mathbf{R}\mathbf{h} = \mathbf{q}. \quad (\text{A-7})$$

The coefficients of the $(2N + 1) \times (2M + 1)$ autocorrelation matrix \mathbf{R} are given by

$$R_{ij} = r_{|i-j|}, \quad (\text{A-8})$$

where r_k denotes the k th lag of the autocorrelation of g , and $N + 1$ is the maximum correlation length.

In order to take the symmetry conditions into account, we partition \mathbf{q} , \mathbf{h} , and \mathbf{R} :

$$\mathbf{h} = \begin{pmatrix} \mathbf{h}^- \\ \mathbf{h}^+ \end{pmatrix}, \quad \mathbf{q} = \begin{pmatrix} \mathbf{q}^- \\ \mathbf{q}^+ \end{pmatrix}, \quad (\text{A-9})$$

and

$$\mathbf{R} = \begin{pmatrix} \mathbf{R}^{--} & \mathbf{R}^{-+} \\ \mathbf{R}^{+-} & \mathbf{R}^{++} \end{pmatrix}. \quad (\text{A-10})$$

The partitioned vectors are given by:

$$\mathbf{h}^- = [h_0/2 \ h_{-1} \ h_{-2} \ \dots \ h_{-M}]^T, \quad (\text{A-11})$$

$$\mathbf{h}^+ = [h_0/2 \ h_1 \ h_2 \ \dots \ h_M]^T, \quad (\text{A-12})$$

$$\mathbf{q}^- = [q_0 \ q_{-1} \ q_{-2} \ \dots \ q_{-N}]^T, \quad (\text{A-13})$$

$$\mathbf{q}^+ = [q_0 \ q_1 \ q_2 \ \dots \ q_N]^T, \quad (\text{A-14})$$

and the submatrices of \mathbf{R} read as

$$\mathbf{R}^{++} = \mathbf{R}^{--} = \begin{pmatrix} r_0 & r_1 & r_2 & \dots & r_M \\ r_1 & r_0 & r_1 & \ddots & r_{M-1} \\ r_2 & r_1 & r_0 & \ddots & r_{M-2} \\ \vdots & \ddots & \ddots & \ddots & \vdots \\ r_N & & & & r_1 & r_0 \end{pmatrix} \quad (\text{A-15})$$

and

$$\mathbf{R}^{-+} = \mathbf{R}^{+-} = \begin{pmatrix} r_0 & r_1 & r_2 & \dots & r_M \\ r_1 & r_2 & r_3 & \ddots & r_{M+1} \\ r_2 & r_3 & r_4 & \ddots & r_{M+2} \\ \vdots & \ddots & \ddots & \ddots & \vdots \\ r_N & & & & r_{M+N-1} & r_{M+N} \end{pmatrix}. \quad (\text{A-16})$$

Note that an additional row and column are added in the system of equations because the coefficients q_0 and $h_0/2$ appear both in the positive and negative parts of the partitioned vectors. It can be verified that equation A-7 can be rewritten in

partitioned form as

$$\begin{pmatrix} \mathbf{R}^{-,+} & \mathbf{R}^{-,-} \\ \mathbf{R}^{+,-} & \mathbf{R}^{+,+} \end{pmatrix} \begin{pmatrix} \mathbf{h}^- \\ \mathbf{h}^+ \end{pmatrix} = \begin{pmatrix} \mathbf{q}^- \\ \mathbf{q}^+ \end{pmatrix}. \quad (\text{A-17})$$

For a symmetric filter, $\mathbf{h}^- = \mathbf{h}^+$, hence equation A-17 reduces to

$$(\mathbf{R}^{+,+} + \mathbf{R}^{+,-})\mathbf{h}^+ = \frac{\mathbf{q}^+ + \mathbf{q}^-}{2}, \quad (\text{A-18})$$

whereas for an antisymmetric filter, $\mathbf{h}^- = -\mathbf{h}^+$. This gives

$$(\mathbf{R}^{+,+} - \mathbf{R}^{+,-})\mathbf{h}^+ = \frac{\mathbf{q}^+ - \mathbf{q}^-}{2}. \quad (\text{A-19})$$

These systems of equations can be solved for the independent filter coefficients using a damped least-squares solution. Prewhitening of the data is essential to avoid artifacts resulting from limited bandwidth.

REFERENCES

- Aki, K., and P. G. Richards, 2002, Quantitative seismology, 2nd ed.: University Science Books.
- Ammon, C. J., 1991, The isolation of receiver effects from teleseismic P waveforms: Bulletin of the Seismological Society of America, **81**, 2504–2510.
- Aritman, B. C., 2001, Repeatability study of seismic source signatures: Geophysics, **66**, 1811–1817.
- Bachrach, R., and A. M. Nur, 1998, High-resolution shallow-seismic experiments in sand, Part I: Water table, fluid flow, and saturation: Geophysics, **63**, 1225–1233.
- Bachrach, R., J. Dvorkin, and A. M. Nur, 1998, High-resolution shallow-seismic experiments in sand, Part II: Velocities in shallow unconsolidated sand: Geophysics, **63**, 1234–1240.
- Baker, G. S., D. W. Steeples, and C. Schmeissner, 1999, In-situ, high-resolution P-wave velocity measurements within 1 m of the earth's surface: Geophysics, **64**, 323–325.
- Birkelo, B. A., D. W. Steeples, R. D. Miller, and M. Sophocleous, 1987, Seismic reflection study of a shallow aquifer during a pumping test: Ground Water, **25**, 703–709.
- Bourbié, T., O. Coussy, and B. Zinszner, 1987, Acoustics of porous media: Technip.
- Curtis, A., and J. O. A. Robertsson, 2002, Volumetric wavefield recording and wave equation inversion for near-surface material properties: Geophysics, **67**, 1602–1611.
- Dankbaar, J. W. M., 1985, Separation of P- and S-waves: Geophysical Prospecting, **33**, 970–986.
- Doornenbal, J. C., and K. Helbig, 1983, High-resolution seismics on a tidal flat in the Dutch Delta — Acquisition, processing and interpretation: First Break, **1**, 9–20.
- Gilbert, F., and G. E. Backus, 1965, Propagator matrices in elastic wave and vibration problems: Geophysics, **31**, 326–332.
- Goforth, T., and C. Hayward, 1992, Seismic reflection investigations of a bedrock surface buried under alluvium: Geophysics, **57**, 1217–1227.
- Haskell, N., 1953, The dispersion of surface waves in multilayered media: Bulletin of the Seismological Society of America, **43**, 17–34.
- Helmberger, D., and R. A. Wiggins, 1971, Upper mantle structure of Midwestern United States: Journal of Geophysical Research, **76**, 3229–3245.
- Hunter, J. A., S. E. Pullan, R. A. Burns, R. M. Gagne, and R. L. Good, 1984, Shallow seismic reflection mapping of the overburden bedrock interface with the engineering seismograph — Some simple techniques: Geophysics, **49**, 1381–1385.
- Kähler, S., and R. Meissner, 1983, Radiation and receiver pattern of shear and compressional waves as a function of Poisson's ratio: Geophysical Prospecting, **31**, 421–435.
- Krohn, C. E., 1984, Geophone ground coupling: Geophysics, **49**, 722–731.
- Michaels, P., 2002, Identification of subsonic P-waves: Geophysics, **67**, 909–920.
- Muijs, R., K. Holliger, and J. O. A. Robertsson, 2002, Perturbation analysis of an explicit wavefield separation scheme for P- and S-waves: Geophysics, **67**, 1972–1982.
- Robertsson, J. O. A., and A. Curtis, 2002, Wavefield separation using densely deployed three-component single-sensor groups in land surface-seismic recordings: Geophysics, **67**, 1624–1633.
- Robertsson, J. O. A., K. Holliger, A. G. Green, A. Pugin, and R. D. Iaco, 1996, Effects of near-surface wave guides on shallow high-resolution seismic refraction and reflection data: Geophysical Research Letters, **23**, 495–498.
- Steeple, D. W., and R. D. Miller, 1990, Seismic reflection methods applied to engineering, environmental and groundwater problems, in S. H. Ward, ed., Geotechnical and environmental geophysics I: SEG, 1–30.
- Stümpel, H., S. Kähler, R. Meissner, and B. Milkereit, 1984, The use of seismic shear waves and compressional waves for lithological problems of shallow sediments: Geophysical Prospecting, **32**, 662–675.
- Thomson, W. T., 1950, Transmission of elastic waves through a stratified solid medium: Journal of Applied Physics, **21**, 89–93.
- Trampert, J., M. Cara, and M. Frogneux, 1993, SH propagator matrix and Q_s estimates from borehole- and surface-recorded earthquake data: Geophysical Journal International, **112**, 290–299.
- Van Vossen, R., J. Trampert, and A. Curtis, 2004, Propagator and wave-equation inversion for near-receiver material properties: Geophysical Journal International, **157**, 796–812.
- Verschuur, D. J., A. J. Berkhout, and C. P. A. Wapenaar, 1992, Adaptive surface-related multiple elimination: Geophysics, **57**, 1166–1177.
- Wapenaar, C. P. A., P. Herrmann, D. J. Verschuur, and A. J. Berkhout, 1990, Decomposition of multicomponent seismic data into primary P- and S-wave responses: Geophysical Prospecting, **38**, 633–661.
- Ward, S. H., 1990, Geotechnical and environmental geophysics, vol. I–III: SEG.
- Yilmaz, O., 2001, Seismic data analysis I — Processing, inversion and interpretation of seismic data: SEG.

Propagator and wave-equation inversion for near-receiver material properties

R. van Vossen,¹ J. Trampert¹ and A. Curtis^{2,3}

¹Faculty of Earth Sciences, Utrecht University, Utrecht, the Netherlands. E-mail: vossen@geo.uu.nl

²Schlumberger Cambridge Research, High Cross, Cambridge, UK

³School of GeoSciences, Edinburgh University, Edinburgh, UK

Accepted 2004 January 13. Received 2004 January 9; in original form 2003 July 15

SUMMARY

Near-receiver material properties are required for the separation of the recorded wavefield into upgoing and downgoing *P* and *S* waves, and are also important for static time-shift corrections. However, it is difficult, especially in land seismics, to obtain reliable estimates for these local material properties using conventional techniques. We compare three methods for estimating these material properties using a 3-D geophone configuration. The first two methods are based on inversion of the wave equation and can be used on almost all of the recorded wavefield. However, they require that the wavefield is recorded by a dense 3-D receiver group to allow the computation of either spatial wavefield derivatives or interpolants. The third approach is based on the inversion of the vertical wavefield propagator. We present a procedure for estimating this propagator using only two multicomponent geophones, one buried and one positioned at the surface. Propagator estimation and inversion avoids the explicit computation of wavefield derivatives, and is therefore less sensitive to measurement errors than both wave-equation inversion schemes. However, in the form presented it requires the identification of arrivals of incoming waves that are isolated in time, and can only be applied to such data. Noise tests demonstrate that the propagator inversion provides accurate estimates for *P*- and *S*-wave velocities of a near-surface low-velocity layer, and is robust with respect to signal-generated near-surface reverberations. In case of a near-surface velocity gradient, velocities are obtained which are consistent with effective medium velocities.

Key words: land seismics, multicomponent, near-surface, propagator, wave equation, waveform inversion.

1 INTRODUCTION

Most observations of seismic waves are made either at, or very near to, the Earth's surface. Before reliable subsurface information can be retrieved from these recordings, corrections are required for local near-receiver structure, since variations in this structure often cause data perturbations of a similar magnitude to the target signal (e.g. Goupillaud 1961). The variability of the elastic properties close to the measurement surface is due to a variety of geological processes and petrophysical properties, among them porosity, permeability, fractures, the presence of fluids in pores, compaction, diagenesis and metamorphism (Toksöz *et al.* 1976).

Variations in near-receiver elastic properties cause the following complications. First, receiver static variations in the data are receiver-to-receiver traveltime anomalies which occur due to the propagation of most of the seismic energy through the heterogeneous shallow structure. Secondly, poor repeatability of the source signature and changes in the source radiation pattern are also attributed to lateral changes in near-surface material properties (Aritman 2001). Thirdly, lateral variations in free-surface reflectivity cause differences in the amount of reflected and converted energy. This results in amplitude perturbations, especially on horizontal recordings (Kähler & Meissner 1983). Decomposing the recorded wavefield into upgoing and downgoing *P* and *S* waves allows an analysis of these wavefields without the effects of any free-surface interaction (e.g. Dankbaar 1985; Wapenaar *et al.* 1990). However, to perform wavefield decomposition the free-surface reflectivity, and hence local subreceiver properties, need to be known.

Since conventional seismic data are acquired only at the surface, the problem of determining seismic subsurface properties is ill-posed. Curtis & Robertsson (2002) therefore proposed to use dense 3-D recording patterns to better constrain land seismic near-surface velocities. The pattern consists of a single buried three-component geophone and several surface geophones. The receivers are sufficiently close that spatial wavefield derivatives can be computed. These derivatives are required to invert the equation of motion for local material parameters.

Robertsson & Muzyert (1999) originally introduced this recording geometry to accomplish P/S separation by explicitly computing the divergence and the curl of the wavefield.

In other research fields, e.g. medical imaging, several concepts to estimate local material properties have been developed. Medical practitioners aim to estimate local material properties since variations in the mechanical properties of tissue often reflect early stage pathology (Gao *et al.* 1996). Unlike in conventional seismic surveys, the displacement field is measured throughout a tissue using measurement techniques based on ultrasound or magnetic resonance imaging (MRI) (Muthupillai *et al.* 1995). Quantitative elasticity reconstruction is achieved either by comparing modelled stress to measured strain (Gao *et al.* 1996; Van Houten *et al.* 1999) or by direct inversion of the observed displacement field. For example, Romano *et al.* (1998) and Oliphant *et al.* (1999, 2001) have shown that elastic properties can be estimated by localized inversion of the equation of motion.

We propose an alternative method to estimate local near-surface P - and S -wave velocities. This method was originally proposed by Trampert *et al.* (1993) to estimate the S -wave velocity structure and the quality factor in a borehole. This was achieved by estimating and inverting the vertical SH wavefield propagator derived from the spectral ratio of a downhole data record over a surface data record. We formulate this approach for the elastic P - SV case and a strategy for inverting the propagator for near-surface P - and S -wave velocities is developed.

Before discussing propagator estimation and inversion, we briefly review techniques based on direct inversion of the wave equation, including those from medical fields. For the purpose of comparison, we illustrate the importance of two of the methods and our propagator inversion method using signals perturbed by noise.

2 WAVE-EQUATION INVERSION

Oliphant *et al.* (1999, 2001) and Curtis & Robertsson (2002) proposed to constrain local material properties by algebraic inversion of the wave equation. A Cartesian coordinate system (x_1, x_2, x_3) is used with the positive vertical direction $z = x_3$ oriented downwards. The particle velocity is regarded as a function of space and time t , and is written as $\mathbf{v} = \mathbf{v}(\mathbf{x}, t)$. Overdots are used to indicate time derivatives (e.g. $\dot{\mathbf{v}} = \partial \mathbf{v} / \partial t$ and $\ddot{\mathbf{v}} = \partial^2 \mathbf{v} / \partial t^2$). The wave equation for \mathbf{v} in a homogeneous, isotropic medium is then given by (Aki & Richards 2002):

$$\ddot{\mathbf{v}} = \alpha^2 \nabla (\nabla \cdot \mathbf{v}) - \beta^2 \nabla \times (\nabla \times \mathbf{v}), \quad (1)$$

where $\alpha = [(\lambda + 2\mu)/\rho]^{1/2}$ is the P -wave velocity, $\beta = (\mu/\rho)^{1/2}$ is the S -wave velocity, and λ and μ are the Lamé parameters. Derivative conditions can be derived from the constitutive equation and the free-surface boundary conditions. The constitutive equation for a homogeneous, elastic medium reads:

$$\sigma_{ij} = \lambda \partial_k v_k \delta_{ij} + \mu (\partial_i v_j + \partial_j v_i), \quad (2)$$

where δ_{ij} is the Kronecker delta and ∂_k denotes the spatial derivative with respect to coordinate x_k . Boundary conditions state that the traction σ_{i3} vanishes at the free surface for $i = 1, 2, 3$, although in practice this is only an approximation, as air waves can exist. By setting $\sigma_{i3} = 0$ at the free surface, we can substitute for vertical wavefield derivative expressions with horizontal derivatives:

$$\partial_3 v_1 = -\partial_1 v_3, \quad (3)$$

$$\partial_3 v_2 = -\partial_2 v_3, \quad (4)$$

$$\partial_3 v_3 = -\left(\frac{\alpha^2 - 2\beta^2}{\alpha^2}\right) (\partial_1 v_1 + \partial_2 v_2). \quad (5)$$

Curtis & Robertsson (2002) showed that the following system of equations is obtained after substitution of the free-surface derivative conditions into the wave equation:

$$\ddot{v}_1 = \beta^2 A_1(t) - \alpha^{-2} \beta^4 B_1(t), \quad (6)$$

$$\ddot{v}_2 = \beta^2 A_2(t) - \alpha^{-2} \beta^4 B_2(t), \quad (7)$$

$$\ddot{v}_3 = \alpha^2 A_3(t) - \beta^2 B_3(t). \quad (8)$$

Expressions for the measurable coefficients A_i and B_i are given in Appendix A. These coefficients require the evaluation of spatial wavefield derivatives. A receiver group as illustrated in Fig. 1 allows the computation of these spatial and temporal derivatives using finite-difference operators (assuming that $v_2 = 0$ and $\partial_2 \mathbf{v} = \partial_{22} \mathbf{v} = 0$). The spatial derivatives can only be obtained accurately if the horizontal and vertical geophone spacings Δx and Δz satisfy the following criteria: $\Delta z \sim \lambda_z^{\min}/6$ and $\Delta x \sim \lambda_x^{\min}/6$, where λ_x^{\min} and λ_z^{\min} are the minimum effective wavelengths in the x or z direction, respectively (Levander 1988; Muijs *et al.* 2002). Assuming that these spatial derivatives can be calculated, eqs (6)–(8) can be inverted for α and β . The attractiveness of this method is that it can deal with the complete wavefield (Curtis & Robertsson 2002). On the other hand, it requires the computation of second-order derivatives which are likely to be affected by noise and measurement errors (Muijs *et al.* 2002).

Romano *et al.* (1998, 2000) suggested to transform the wave eq. (1) into an integral equation to avoid the computation of spatial wavefield derivatives. This approach is referred to as the variational formulation, and we present it for estimating local near-surface material properties

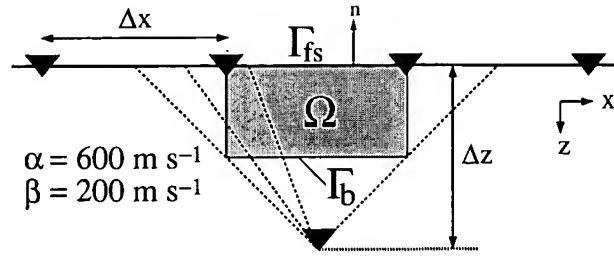


Figure 1. Geophone configuration for near-surface velocity estimation. The volume Ω bounded by surface $\Gamma = \Gamma_b \cup \Gamma_{fs}$ with outward-pointing normal vector \mathbf{n} is used in the variational formulation. Wavefield interpolation is performed along the dashed lines.

using the geophone configuration shown in Fig. 1. Consider a vector-valued function \mathbf{w} and a volume Ω bounded by a surface Γ with outward-pointing normal vector \mathbf{n} (Fig. 1). In Appendix B, we demonstrate that eq. (1) is equivalent to

$$\int_{\Omega} d\Omega \mathbf{w} \cdot \ddot{\mathbf{v}} = \int_{\Omega} d\Omega \mathbf{v} \cdot \mathbf{w}_{\Omega} + \int_{\Gamma} d\Gamma \mathbf{n} \cdot \mathbf{w}_{\Gamma}, \quad (9)$$

where

$$\mathbf{w}_{\Omega} = \alpha^2 \nabla(\nabla \cdot \mathbf{w}) - \beta^2 \nabla \times (\nabla \times \mathbf{w}), \quad (10)$$

$$\mathbf{w}_{\Gamma} = (\alpha^2 - \beta^2)[\mathbf{w}(\nabla \cdot \mathbf{v}) - \mathbf{v}(\nabla \cdot \mathbf{w})] - \beta^2[\mathbf{v} \cdot (\nabla \mathbf{w})^T - \mathbf{w} \cdot (\nabla \mathbf{v})^T]. \quad (11)$$

Eq. (9) is known as Betti's theorem (Ben-Menahem & Singh 1981).

The surface $\Gamma = \Gamma_b \cup \Gamma_{fs}$, where Γ_{fs} is the surface of Ω which coincides with the free surface (see Fig. 1). Because the vector-valued function \mathbf{w} can be chosen arbitrarily, boundary conditions can be imposed on \mathbf{w} to aid the computation of the integrals in eq. (9). If we assume that

$$\mathbf{w} = \mathbf{0} \quad \text{on } \Gamma_b \quad (12)$$

and

$$(\nabla \mathbf{w})^T \cdot \mathbf{n} = \mathbf{0} \quad \text{on } \Gamma_b, \quad (13)$$

the contribution of the surface integral along Γ_b vanishes. The evaluation of the surface integral along Γ_{fs} requires the computation of first-order spatial wavefield derivatives at the free surface. These are also needed for accurate wavefield interpolation throughout Ω : first, the wavefield and its horizontal derivative are interpolated along the free surface using B-splines (Unser 1999). Secondly, the vector gradient of the wavefield is obtained using the free-surface conditions (eqs 3–5). Next, the wavefield in Ω is interpolated along lines from the surface to the buried geophone (the dashed lines in Fig. 1). The interpolated wavefield is parametrized by second-order polynomials, which are uniquely determined by the interpolated wavefield at the free surface, the directional derivative at the free surface and the wavefield at depth Δz . For sufficiently accurate wavefield interpolation within volume Ω , we found that, similar to the previous method, $\Delta z \sim \lambda_z^{\min}/6$ and $\Delta x \sim \lambda_x^{\min}/6$. Finally, the surface and volume integrals are evaluated using the trapezium rule.

Consider the following independent vector-valued functions:

$$\mathbf{w}_1 = (f_w, 0, 0)^T, \quad (14)$$

$$\mathbf{w}_2 = (0, 0, f_w)^T, \quad (15)$$

with

$$f_w(x_l, z_l) = (x_l^4 - 2x_l^2 + 1)(z_l - 1)^2. \quad (16)$$

The local coordinates x_l and z_l are related to x and z according to:

$$x_l = 2x/\Delta x_{\Omega}, \quad (17)$$

$$z_l = (2z - \Delta z_{\Omega})/\Delta z_{\Omega}, \quad (18)$$

with Δx_{Ω} and Δz_{Ω} the lengths of the sides of volume Ω . The local coordinates are defined on the domain $x_l \in [-1, 1]$ and $z_l \in [-1, 1]$. The functions \mathbf{w}_1 and \mathbf{w}_2 satisfy the boundary conditions (eqs 12 and 13).

We illustrate both methods with a 2-D example. Synthetic data for a half-space model are computed using the Cagniard-de Hoop method (de Hoop & van der Hijden 1983). An explosive line source oriented in the x_2 direction is located at 200 m depth and emits a Ricker wavelet with a dominant frequency of 40 Hz. The P -wave velocity is 600 m s⁻¹, the S -wave velocity is 200 m s⁻¹, and the density is 1600 kg m⁻³. Multicomponent geophones are centred around 50 m offset. The horizontal geophone spacing $\Delta x = 1.0$ m and the buried geophone is located at 0.50 m depth. For a Ricker wavelet with a 40 Hz dominant frequency, the maximum frequency f_{\max} with significant energy is 80 Hz.

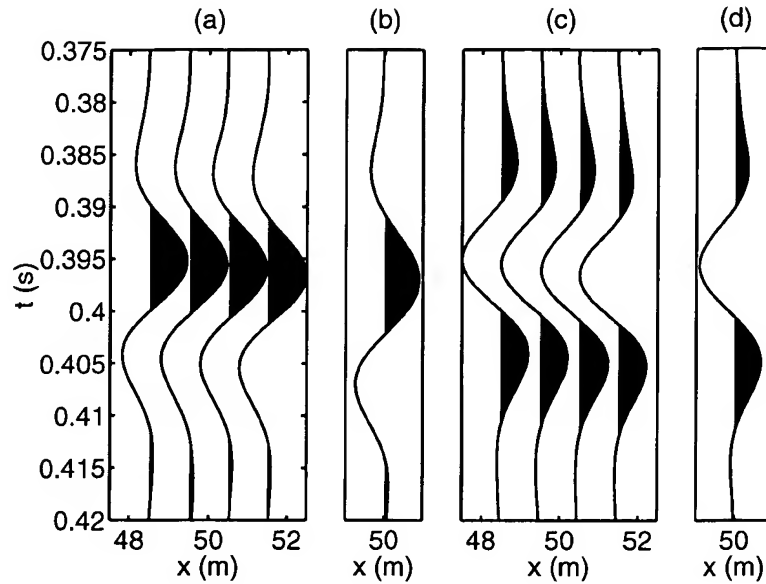


Figure 2. Synthetic data traces for (a) v_x at the surface, (b) v_x at depth Δz , (c) v_z at the surface and (d) v_z at depth Δz .

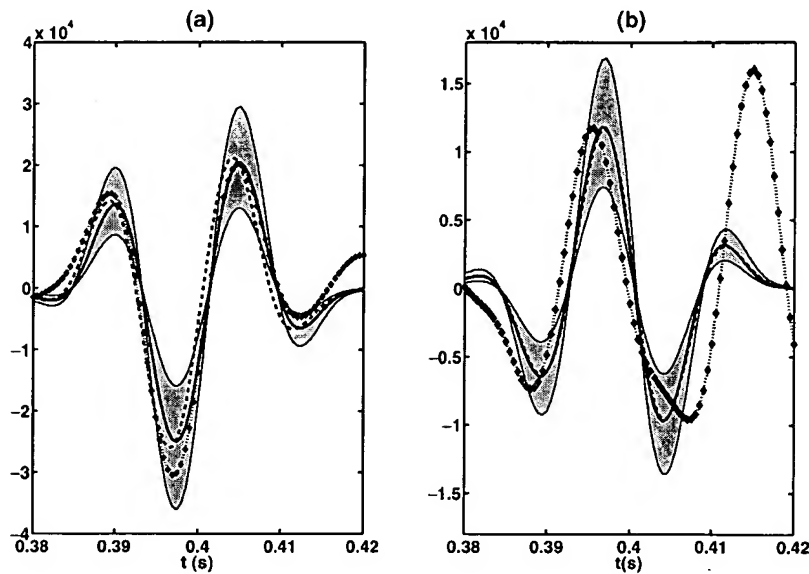


Figure 3. Sensitivity analysis for direct wave-equation inversion. (a) The waveforms of the left (dashed) and right side (solid line) of eq. (6), and the grey area illustrates the region for ± 20 per cent perturbations in β . The dotted line shows the effect of Gaussian noise (25 dB S/N ratio) added to the velocity recordings on the right side of eq. (6). Similarly, (b) shows the waveforms of eq. (8) and illustrates the region for ± 20 per cent perturbations in α . The dotted line shows the effect of Gaussian noise (25 dB S/N ratio) added to the velocity recordings.

Then, the minimum wavelength $\lambda_{\min} = c_{\min}/f_{\max} = 2.5$ m, with c_{\min} the minimum phase velocity. The geophone configuration satisfies the wavelength condition for the computation of derivatives and interpolants. The length of the sides of Ω are $\Delta x_{\Omega} = \Delta x$ and $\Delta z_{\Omega} = \Delta z/2$ (Fig. 1). Recorded data are shown in Fig. 2.

The constraints of direct wave-equation inversion on α and β are illustrated in Fig. 3. For the given model values α and β , there is a good match between the left and right side of eqs (6) and (8). For noise-free data, derivative operators are obtained sufficiently accurately with the geophone configuration of Fig. 1. Perturbing α or β results in amplitude changes in the waveforms of the right-side terms in eqs (6)–(8). We compare the sensitivity to perturbations in α and β with the effect of measurement errors in the particle velocity recordings. To study these effects, 25 dB uncorrelated Gaussian noise (peak-to-peak energy signal-to-noise (S/N) ratio) was added to the velocity recordings. A bandpass filter ($20 \text{ Hz} < f < 100 \text{ Hz}$) was applied to these recordings before computing the wavefield derivatives. As a result, the effect of noise on temporal wavefield derivatives is reduced. However, spatial wavefield derivatives are still severely distorted by the added noise.

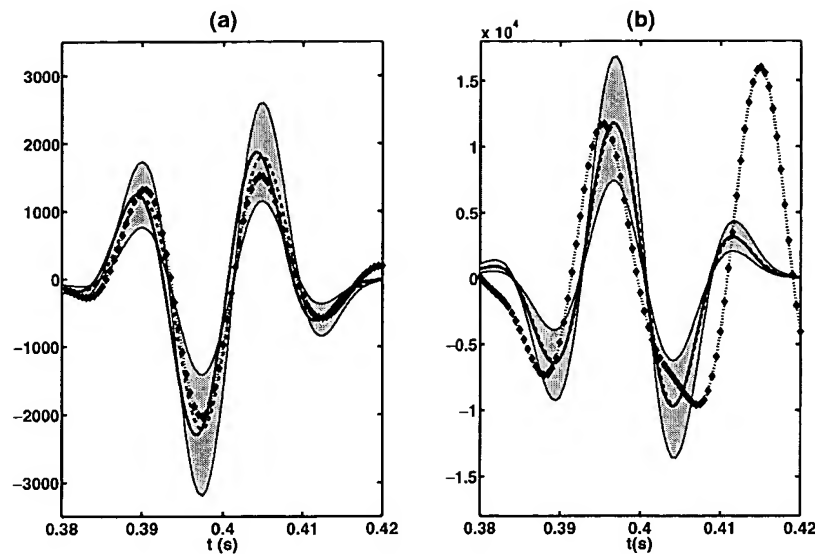


Figure 4. Sensitivity analysis for the variational formulation. The waveforms of the left (dashed) and right side (solid line) of eq. (9) are shown for w_1 (a) and w_2 (b). The grey area in (a) illustrates the region for ± 20 per cent perturbations in β , whereas (b) shows this region for ± 20 per cent perturbations in α . The dotted curves show the effect of Gaussian noise (25 dB S/N ratio) added to the velocity recordings.

Estimates for α are especially affected, since the wavelength for P waves is larger than for S waves. Consequently, the S/N ratio for spatial P -wave derivatives is lower than for S -wave derivatives.

Fig. 4 shows a similar analysis for the variational approach. There is a good agreement between the left and right side of equation (9) for the given model values α and β . In principle, the interpolation and integration steps are sufficiently accurate using the geophone configuration shown in Fig. 1. Perturbing α or β results in amplitude changes in the waveforms of the right side terms in eq. (9). A comparison between the sensitivity to α and β and the effects of noise (25 dB S/N ratio) shows that this approach is also very sensitive to the effects of noise, and again mostly for α .

These sensitivity tests demonstrate that it may only be possible to constrain β using these methods. There is not a clear difference between the derivative and variational formulation. However, for a geophone configuration with more than one buried geophone, an interpolation scheme can be developed which is less sensitive to random errors.

Muijs *et al.* (2002) studied the effect of deployment-related errors, such as misorientation and mislocation of geophones in a 3-D recording geometry, on the computation of divergence and curl. These are particularly sensitive to misorientations of geophones, requiring that the orientations of all geophones be accurate within 2° .

Instead of using the full wave equation, the free-surface condition given in eq. (5) can be used to determine a velocity ratio between α and β (Curtis & Robertsson 2002). This only requires the computation of first-order spatial wavefield derivatives, and is therefore expected to be more robust than wave-equation inversion. Both the free-surface conditions and wave-equation inversion are applicable to the complete wavefield, except the airwave.

As an alternative, we propose a new method which avoids the explicit computation of spatial wavefield derivatives and imposes no requirements on the maximum depth separation of geophones. This is achieved by assuming that the incident wavefield can be described by a single plane wave.

3 PROPAGATOR ESTIMATION

Our alternative approach to wave-equation inversion is based on propagator inversion. Trampert *et al.* (1993) proposed estimating the S -wave velocity structure and the quality factor by analysing the vertical SH propagator in the time domain. The propagator contains all information on the material properties between the free surface and the depth of a buried geophone, and can be estimated directly from recorded data. The S velocity can be constrained by determining the time lag between the peaks in the SH propagator. This time difference represents the two-way traveltime of an SH wave to depth Δz . The amplitude difference between the peaks can be used to infer the quality factor: downward continuation of upgoing waves results in increasing amplitudes, whereas the amplitudes of downgoing waves decrease with depth.

We generalize this procedure to estimate the elastic P - SV propagator and illustrate a scheme to constrain near-surface P - and S -wave velocities based on waveform inversion of this P - SV propagator.

Assuming a plane wave solution for the wave equation, the plane wave at depth Δz can be written in the form

$$\mathbf{v}(t, x, \Delta z) = \mathbf{P}(t, x) * \mathbf{v}(t, x, 0), \quad (19)$$

where

$$\mathbf{P} = \begin{pmatrix} P_{11} & P_{12} & P_{13} \\ P_{21} & P_{22} & P_{23} \\ P_{31} & P_{32} & P_{33} \end{pmatrix} \quad (20)$$

and * denotes a temporal convolution. For a homogeneous, isotropic and elastic medium between the free surface and depth Δz , the propagator \mathbf{P} is a function of the P -wave velocity α , the S -wave velocity β and the horizontal slowness p . For a free-surface incident plane wave with slowness p , the theoretical propagator coefficients read (Aki & Richards 2002):

$$\hat{P}_{11} = \beta^2 p^2 G_1^P + [(1 - 2\beta^2 p^2)/2] G_1^S, \quad (21)$$

$$\hat{P}_{22} = G_1^S, \quad (22)$$

$$\hat{P}_{33} = [(1 - 2\beta^2 p^2)/2] G_1^P + \beta^2 p^2 G_1^S, \quad (23)$$

$$\hat{P}_{13} = [p(1 - 2\beta^2 p^2)/(2q_P)] G_2^P - \beta^2 p q_S G_2^S, \quad (24)$$

$$\hat{P}_{31} = \beta^2 p q_P G_2^P - [p(1 - 2\beta^2 p^2)/(2q_S)] G_2^S, \quad (25)$$

$$\hat{P}_{12} = \hat{P}_{21} = \hat{P}_{23} = \hat{P}_{32} = 0, \quad (26)$$

where

$$G_1^P(t, p) = [\delta(t + q_P \Delta z) + \delta(t - q_P \Delta z)], \quad (27)$$

$$G_2^P(t, p) = [\delta(t + q_P \Delta z) - \delta(t - q_P \Delta z)], \quad (28)$$

$$G_1^S(t, p) = [\delta(t + q_S \Delta z) + \delta(t - q_S \Delta z)], \quad (29)$$

$$G_2^S(t, p) = [\delta(t + q_S \Delta z) - \delta(t - q_S \Delta z)]. \quad (30)$$

The vertical slownesses q_P and q_S are given by:

$$q_P = (\alpha^{-2} - p^2)^{1/2}, \quad (31)$$

$$q_S = (\beta^{-2} - p^2)^{1/2}. \quad (32)$$

Eqs (27)–(30) contain the phase shifts for two-way extrapolation of the wavefield towards depth Δz . Positive phase shifts describe the propagation of downgoing waves to Δz , whereas negative phase shifts indicate propagation of upgoing waves to this depth.

The coefficients of the propagator matrix (eqs 21–26) can be interpreted as follows. Extrapolation of P – SV waves is described by P_{11} , P_{13} , P_{31} and P_{33} , whereas for SH waves it is given by P_{22} . The amplitude terms before G_1^P , G_1^S , G_2^P and G_2^S are wavefield decomposition filters: the wavefield is separated into P , SV and SH waves before extrapolating the recordings to depth Δz , which is given by the phase terms. Finally, summation of the extrapolated decomposed wavefield renders the total wavefield at depth Δz (Osen *et al.* 1999; Aki & Richards 2002).

In the case of a non-attenuating medium, the extrapolation filters for elastic P – SV wave propagation can be obtained directly from the data by exploiting symmetry properties of the filters: the theoretical expressions for the extrapolation filters show that P_{11} , P_{22} and P_{33} are even functions around $t = 0$ and P_{13} and P_{31} are odd functions. Hence, the spectra of P_{11} , P_{22} and P_{33} are entirely real, whereas the spectra of P_{13} and P_{31} are purely imaginary. These properties are used to estimate the extrapolation filters without prior information on α , β and p . Equating real and imaginary parts of eq. (19) in the frequency domain shows that the propagator coefficients are given by:

$$P_{11} = \{\Re[v_3(\omega, x, 0)]\Re[v_1(\omega, x, \Delta z)] + \Im[v_3(\omega, x, 0)]\Im[v_1(\omega, x, \Delta z)]\}/D(\omega), \quad (33)$$

$$P_{33} = \{\Re[v_1(\omega, x, 0)]\Re[v_3(\omega, x, \Delta z)] + \Im[v_1(\omega, x, 0)]\Im[v_3(\omega, x, \Delta z)]\}/D(\omega), \quad (34)$$

$$P_{13} = i\{\Re[v_1(\omega, x, 0)]\Im[v_3(\omega, x, \Delta z)] - \Im[v_1(\omega, x, 0)]\Re[v_3(\omega, x, \Delta z)]\}/D(\omega), \quad (35)$$

$$P_{31} = i\{\Re[v_3(\omega, x, 0)]\Im[v_1(\omega, x, \Delta z)] - \Im[v_3(\omega, x, 0)]\Re[v_1(\omega, x, \Delta z)]\}/D(\omega), \quad (36)$$

where

$$D(\omega) = \Re[v_3(\omega, x, 0)]\Re[v_1(\omega, x, 0)] + \Im[v_3(\omega, x, 0)]\Im[v_1(\omega, x, 0)]. \quad (37)$$

In these equations, $\Re[v(\omega, x, z)]$ denotes the real part of $v(\omega, x, z)$ and $\Im[v(\omega, x, z)]$ is the imaginary part of $v(\omega, x, z)$. Expressions for $\mathbf{P}(t, x)$ are found by taking the inverse Fourier transform of eqs (33)–(36). Note that these symmetry properties break down for the P – SV case in the presence of attenuation. Then, only the SH case can be treated correctly (Trampert *et al.* 1993). The propagator estimation procedure remains valid in a vertically inhomogeneous medium.

The following procedure is used to stabilize the spectral divisions in eqs (33)–(37). For arbitrary signals $F(\omega)$ and $D(\omega)$, the spectral division of $F(\omega)$ by $D(\omega)$ is given by:

$$G(\omega) = \frac{F(\omega)}{D(\omega)}. \quad (38)$$

Unfortunately, spectral division is numerically unstable both because signals are band-limited and due to the existence of low-amplitude notches in the spectrum. In practice, the spectral ratio is estimated using the following technique (Helmberger & Wiggins 1971; Langston 1979):

$$G'(\omega) = \frac{F(\omega)D^*(\omega)}{\Phi_{DD}(\omega)}W(\omega), \quad (39)$$

where

$$\Phi_{DD} = \max\{D(\omega)D^*(\omega), c \max[D(\omega)D^*(\omega)]\}, \quad (40)$$

and $W(\omega)$ is a frequency window to limit the final frequency band in the estimated deconvolution. The complex conjugate of D is denoted by D^* . The function Φ_{DD} can be thought of as simply being the autocorrelation of $D(\omega)$ with any spectral notches filled to a level depending on the parameter c . The frequency windowing function $W(\omega)$ is a tapered window with cut-off frequencies set to the minimum and maximum frequencies for which

$$D(\omega)D^*(\omega) > c \max[D(\omega)D^*(\omega)]. \quad (41)$$

This criterion implies that the parameter c also controls the bandwidth of the spectral ratio $G'(\omega)$.

4 PROPAGATOR INVERSION

4.1 Half-space example

We shall first illustrate the inversion scheme for near-surface velocities with a half-space example. Synthetic data are computed using the Cagniard–de Hoop method (de Hoop & van der Hijden 1983). We restrict ourselves to the P – SV case since SH was fully treated by Trampert *et al.* (1993). The P -wave velocity is 600 m s^{-1} , the S -wave velocity is 200 m s^{-1} and the density is 1600 kg m^{-3} . An explosive line source is located at 200 m depth and emits a 120 Hz Ricker wavelet. Multicomponent geophones are positioned at 50 m offset, one is located at the free surface and the second geophone is located at 1.0 m depth (Fig. 5). Fig. 6 shows traces recorded by these receivers.

The propagators P_{11} , P_{13} , P_{31} and P_{33} may be estimated from these data. Theoretical solutions for propagator filters are functions of α , β and p . Fig. 7(a) shows these filters for the given model parameters. Before comparing these propagator coefficients with the data-estimated propagator filters, it is necessary to limit the frequency band of these theoretical expressions to the same frequency band as used for the data-estimated propagator filters. The time domain expressions of the frequency windowing functions $W_{ij}(\omega)$ (eq. 39), where W_{ij} are the frequency windowing functions for propagator components P_{ij} , are shown in Fig. 7(b). Fig. 7(c) illustrates the data-estimated and band-limited theoretical propagators.

We choose to invert the propagator for near-surface velocities in the time domain. In this domain, the propagators can be interpreted as follows. The time delay between the peaks in P_{11} and P_{33} gives the two-way vertical traveltime for SV and P waves, and the amplitudes of the propagator filters are controlled by the velocity structure between the free surface and depth Δz and the signal bandwidth. To constrain α , β and p from the propagator waveforms, we define the following objective function:

$$E = E_{11} + E_{33} + E_{13} + E_{31}, \quad (42)$$

with

$$E_{ij} = \left(\sum_{t=t_1}^{t_2} [P_{ij}(t, x) - \hat{P}_{ij}(t, x, \alpha, \beta, p)]^2 \right)^{1/2}. \quad (43)$$

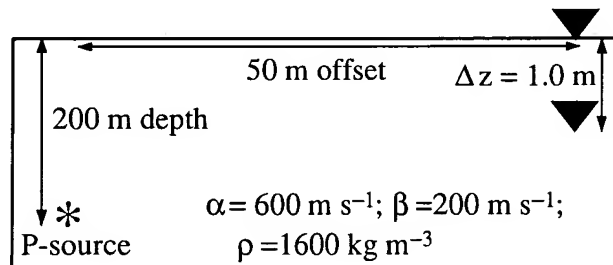


Figure 5. Geophone configuration and parameters of the half-space model.

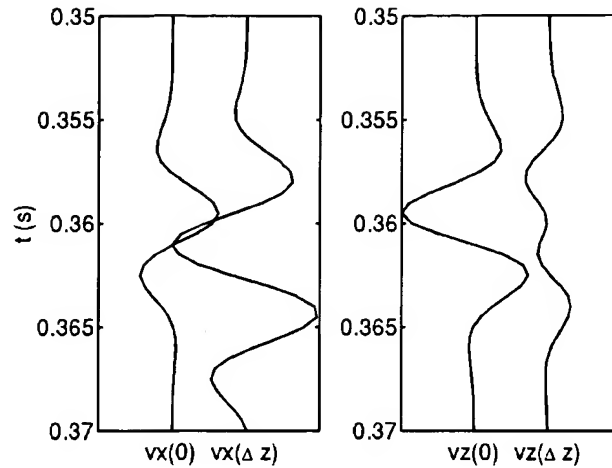


Figure 6. Synthetic traces of the particle velocity recorded by the surface and buried geophone shown in Fig. 5. The left graph shows traces of v_x and the right graph of v_z .

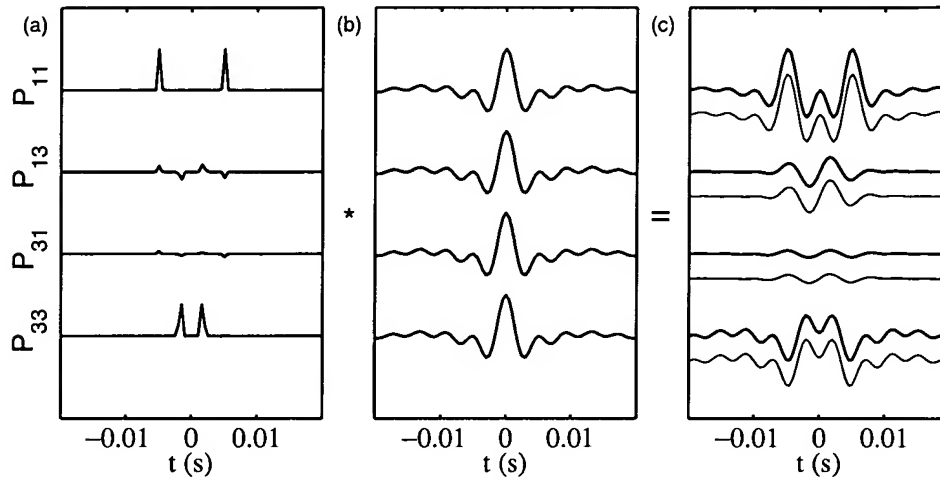


Figure 7. Propagator fitting procedure for the data displayed in Fig. 6. Given estimates for α , β and p , theoretical solutions for the wavefield extrapolation filters can be computed (a). In practice, data are band-limited, and therefore this theoretical solution cannot be compared directly with the estimated filters. (b) The time-domain expressions of frequency filters which limit the solution to the frequency band in which the spectral division was performed. A convolution of the theoretical solution in (a) with the filter shown in (b) allows a comparison with the data-estimated propagator. Part (c) shows that there is a good agreement between the theoretical (thin lines) and data-estimated propagator filters (thick lines). The stabilization factor $c = 1 \times 10^{-3}$.

The theoretical solution for the propagator filter component ij is denoted by $\hat{P}_{ij}(t, x, \alpha, \beta, p)$ and $P_{ij}(t, x)$ is the data-estimated propagator filter component ij . The objective function E is a function in a 3-D model space. Cross-sections of the objective function (Fig. 8) show that perturbations in p have a relatively small influence on estimates of α and β .

So far, we have considered noise-free data. The data-estimated propagator filters for recorded data perturbed by 25 dB uncorrelated Gaussian noise are shown in Fig. 9. These are compared with the theoretical filters for different values of the stabilization factor c (eq. 40), namely $c = 10^{-4}$, $c = 10^{-3}$ and $c = 10^{-2}$. For increasing value of c , the effect of noise is reduced in the propagator filters. Furthermore, the frequency band is more limited for a higher c value. The filters are smoothed and contain less energy.

We estimated the relative variations in α , β and p for different noise levels and c values. To quantify the effect of noise, we define the relative root-mean-square error (RMS) in α by:

$$\text{RMS}(\alpha) = \frac{1}{\alpha_0} \left(\frac{\sum_{i=1}^N (\alpha_i - \alpha_0)^2}{N} \right)^{1/2}, \quad (44)$$

with α_0 the model P -wave velocity and α_i the estimated P -wave velocities, which are found by minimizing E in eq. (42). Similar expressions are defined for the relative RMS error in β and p . For each noise level, experiments were conducted 1000 times ($N = 1000$) with different manifestations of Gaussian noise. The minimum of the objective function E was determined using a forward search method. Fig. 10 shows that the estimates of α , β and p are most robust for $c = 10^{-2}$: c clearly stabilizes noise very systematically. Furthermore, α and β are better constrained than p , which implies that relative errors in estimates of p have less influence on estimates of the other parameters than do relative errors of similar magnitude in either α or β .

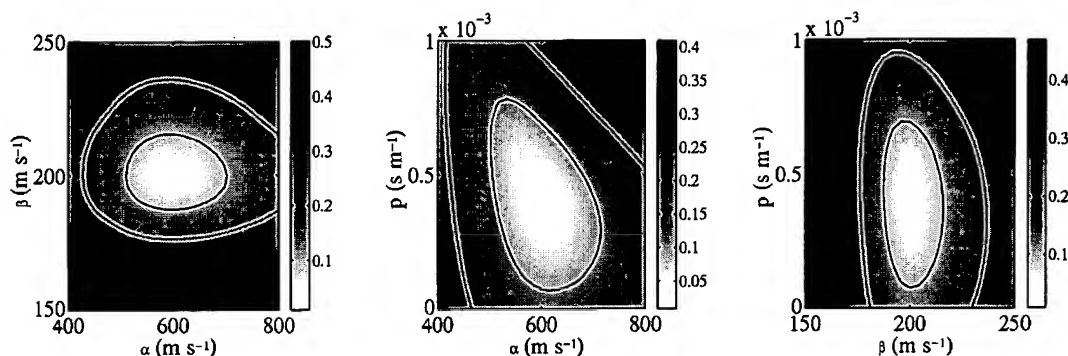


Figure 8. Cross-sections intersecting the minimum of the objective function E . Contours are drawn for $E = 0.10$ and $E = 0.20$.

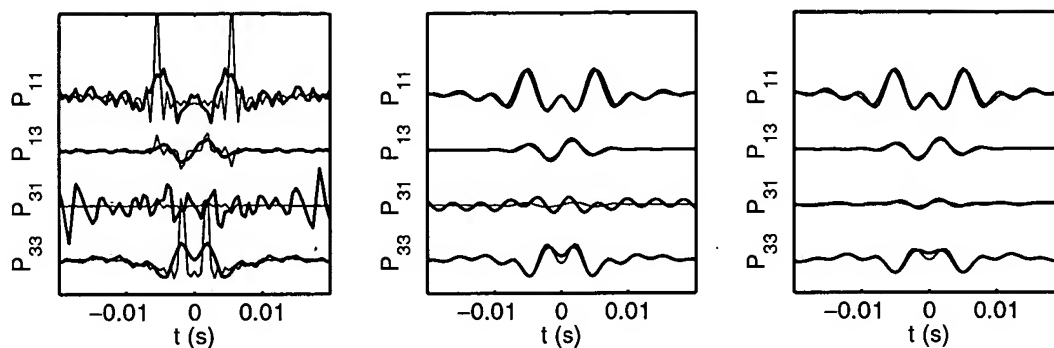


Figure 9. Effect of the stabilization factor c on noise-perturbed propagator filters. The S/N ratio is 25 dB. The propagator filters are computed for $c = 10^{-4}$ (left), $c = 10^{-3}$ (centre) and $c = 10^{-2}$ (right). The thin lines are the band-limited theoretical solutions and the thick lines the data-estimated propagators. The amplitudes of each filter are normalized to the solution for $c = 10^{-4}$. For increasing values of c , the noise is effectively reduced.

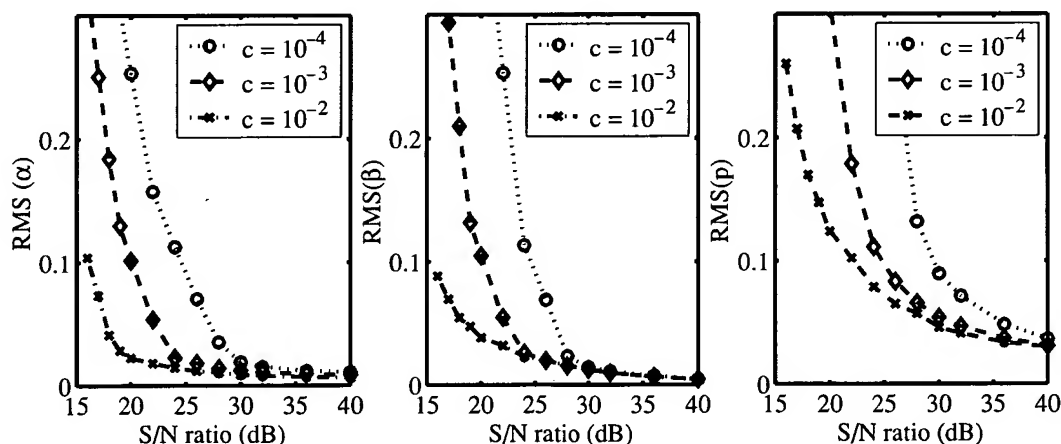


Figure 10. Uncertainties in estimates for α , β and p for different S/N ratios and c values.

In addition to random errors, the effect of position and orientation errors of the geophones within the recording pattern is investigated. We only consider misorientation in the xz -plane, described by rotation angle θ (positive for rotation in clockwise direction). The effects of misorientation and mislocation are quantified with a relative error e . The relative error in α is given by:

$$e(\alpha) = (\alpha - \alpha_0)/\alpha_0. \quad (45)$$

Similar expressions are used for relative errors in β and p . Fig. 11(a) shows the relative error in estimates for α , β and p due to misorientation of the geophone located at the free surface. The errors in α and β are small compared with relative errors in p . Large errors are found for θ close to the angle of incidence. In this example, there are only free-surface incident P waves. This rotation causes the energy on the horizontal recording and thus on the denominator $D(\omega)$ (equation 37) to be minimized. As a consequence, the spectral divisions (eqs 33–36) become

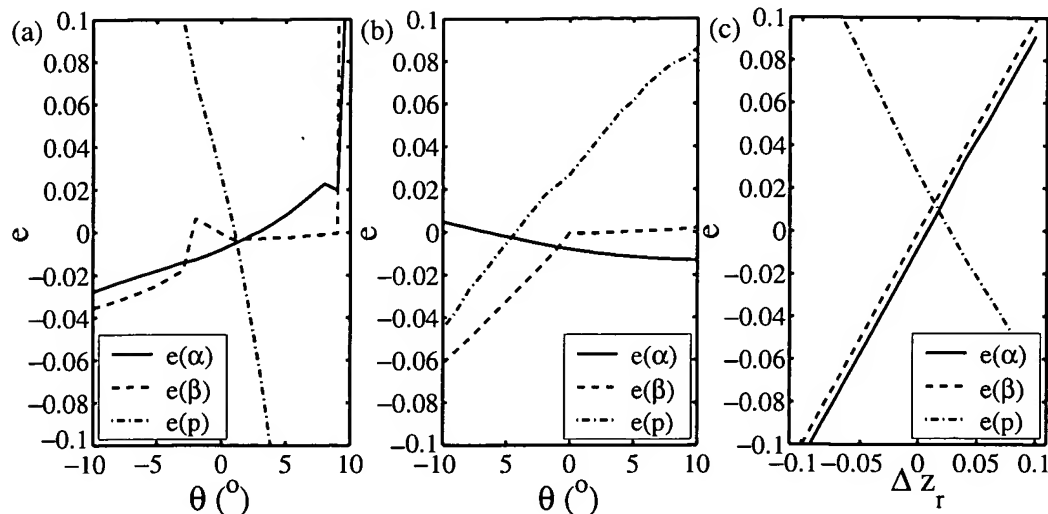


Figure 11. Errors in velocity estimates due to mislocation and misorientation: (a) misorientation in the xz plane of a surface geophone; (b) misorientation in the xz plane of a buried geophone; (c) vertical mislocation of a buried geophone. The stabilization factor $c = 10^{-3}$.

unstable. In the case of near-surface structure, we do not expect such a rapidly increasing error, because in that case both P and S waves will be recorded.

The errors caused by misorientation of the buried geophone is shown in Fig. 11(b). Here, $e(\alpha)$ and $e(\beta)$ remain small, because $v(\omega, \Delta z)$ does not contribute to the denominator $D(\omega)$. Finally, the effect of vertical mislocation of the buried geophone is illustrated in Fig. 11(c)—the values for Δz are changed in the inversion procedure; the relative change in the depth for the buried geophone $\Delta z_r = (\Delta z - \Delta z_0)/\Delta z_0$, with Δz_0 the true depth of the buried geophone. There is a linear relationship between errors in Δz and estimated velocities. This implies that the phase contains most information on the velocities.

It is difficult to make a fair comparison between wave-equation inversion techniques and propagator inversion. Wave-equation inversion uses the *amplitudes* in the wave equation (eq. 1) to constrain α and β . This requires measurement of spatial and temporal wavefield derivatives by a dense 3-D geophone configuration, with a spatial separation on a subwavelength scale. Propagator inversion, on the other hand, uses mainly *phase* information. To estimate time differences reliably, the depth separation between geophones needs to be larger than those used for wave-equation inversion. Therefore, we used different depths for the buried geophone and different dominant frequencies for the source wavelet.

The obtained results suggest that propagator inversion is less sensitive to both random and deployment related data perturbations. For a S/N ratio of 25 dB, propagator inversion gives no error in α and β , whereas for the wave-equation inversion techniques Figs. 3 and 4 indicate more than 20 per cent deviations in estimates for α , while β is still well resolved. Furthermore, Fig. 11 demonstrated that propagator inversion is tolerant to at least 5° misorientations and 5 per cent vertical mislocations of individual geophones. Derivative operators on the other hand are particularly sensitive to random misorientations of geophones. Muijs *et al.* (2002) showed that computation of divergence and curl with dense 3-D recording geometries requires that the orientations of all geophones are accurate within 2° . This criterion needs to be satisfied as well for wave-equation inversion techniques.

Although propagator inversion is tolerant to measurement errors, it is questionable whether this is the dominant source of errors for this method, since a single slowness assumption is implicit in propagator estimation and inversion. Wave-equation inversion techniques do not have this assumption and are applicable to the complete wavefield. In the following experiments, we investigate if propagator inversion is accurate in a model with near-surface structure.

4.2 Low-velocity layer example

The second experiment is performed in a model with a near-surface low-velocity layer. Reverberations in this layer result in multiple arrivals. The near-surface layer is 5 m thick with $\alpha = 600 \text{ m s}^{-1}$, $\beta = 200 \text{ m s}^{-1}$ and $\rho = 1600 \text{ kg m}^{-3}$. The parameters of the underlying half-space are: $\alpha = 1500 \text{ m s}^{-1}$, $\beta = 400 \text{ m s}^{-1}$, and $\rho = 1800 \text{ kg m}^{-3}$. The P -source is located at 100 m depth and emits a 120 Hz Ricker wavelet (see Fig. 12). The receiver group is similar to the previous experiment. Synthetic data are computed with a reflectivity method (Kennett 1983). The recorded synthetic traces are shown in Fig. 13. These clearly show the multiple arrivals due to interfering waves in the near-surface low-velocity layer.

The data-estimated propagators are again compared with the theoretical propagators (Fig. 14). The latter were computed for the horizontal slowness of the first break, which is $3.1 \times 10^{-4} \text{ s m}^{-1}$. Due to the multiple arrivals (multiple horizontal slownesses), there is not an exact match between the theoretical and data-estimated propagators. The energy in the propagator filters decays for higher values of c . For too high a c

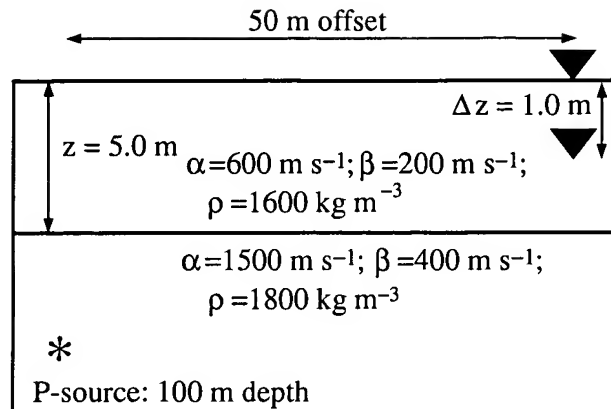


Figure 12. Model and geophone configuration for experiment with a near-surface low-velocity layer.

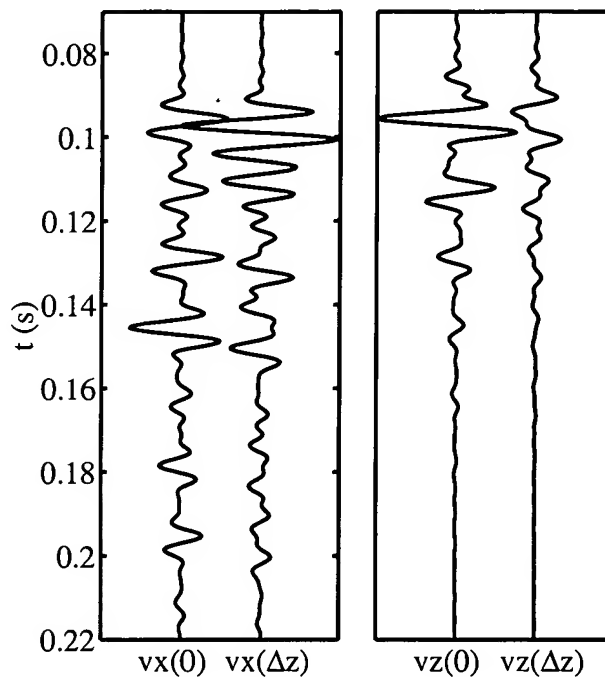


Figure 13. Synthetic traces recorded by the geophone configuration displayed in Fig. 12. Recordings of v_x (left) and v_z are shown (right).

value, the fit between the theoretical and data-estimated propagator deteriorates. This can be attributed to the stabilization of internal notches in $D(\omega)$, whereas the theoretical propagator is not compensated for the energy decay in \mathbf{P} due to this stabilization.

Cross-sections of misfit functions using $c = 10^{-3}$ are shown in Fig. 15. The minimum is located close to the model velocities, whereas the estimated p tends to be smaller than that of the first break, namely around $2.8 \times 10^{-4} \text{ s m}^{-1}$. Waves reverberating in the low-velocity layer arrive at smaller angles of incidence, thus the estimated p can be regarded as some averaged value over all these arrivals.

Fig. 16 illustrates the effects of added noise on velocity and slowness estimation. For high S/N ratios, the estimates for α and β do not exactly converge for $c = 5 \times 10^{-3}$ and $c = 10^{-2}$, as was suggested by Fig. 15 as well. The estimated horizontal slowness differs from that of the direct arrival and varies for different values of c . As in the half-space example, c stabilizes the effects of noise. Reliable estimates for α and β are obtained for S/N ratios down to approximately 18 dB.

4.3 Structure between the surface and the buried geophone

A critical assumption in the propagator inversion scheme is that the medium between the surface and buried geophones is homogeneous. However, according to the classical Hertz–Mindlin model (Mindlin 1949), velocities increase with confining pressure and thus with depth, especially in the top few metres. This also has been observed in field experiments (e.g. Bachrach *et al.* 2000). Here, we consider a model with a large velocity gradient close to the free surface. The velocity gradient decreases with depth (Fig. 17). The gradient model is parametrized by

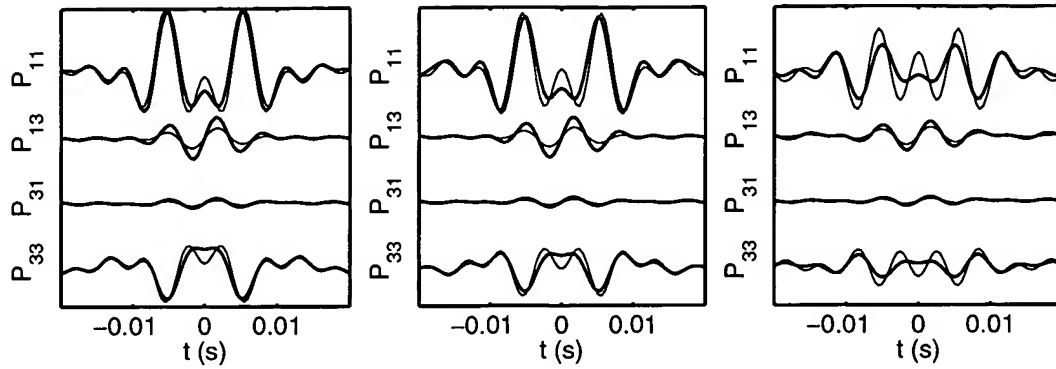


Figure 14. Effect of the stabilization factor c on estimated propagators: $c = 10^{-4}$ (left), $c = 10^{-3}$ (centre) and $c = 10^{-2}$ (right). The thin lines are the theoretical solutions computed with the horizontal slowness of the first break and the thick solid lines are the propagators estimated from the data. Traces are normalized with respect to the $c = 10^{-4}$ curves.

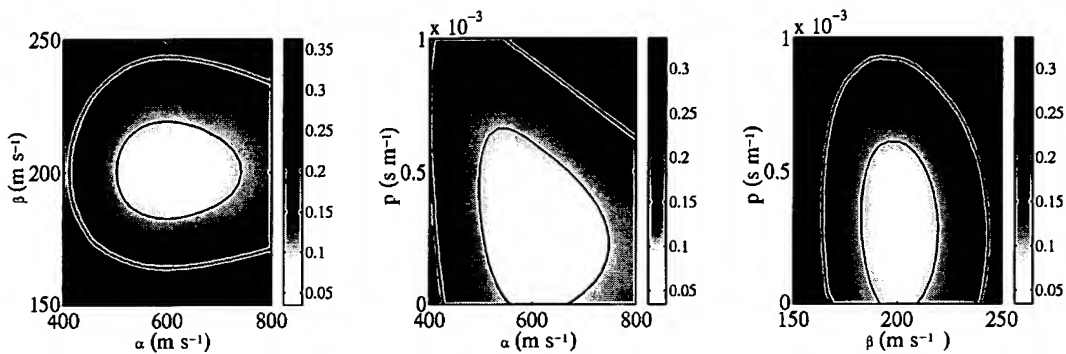


Figure 15. Cross-sections intersecting the minimum of the objective function E for the low-velocity layer model. Contours are drawn for $E = 0.10$ and $E = 0.20$ and $c = 10^{-3}$.

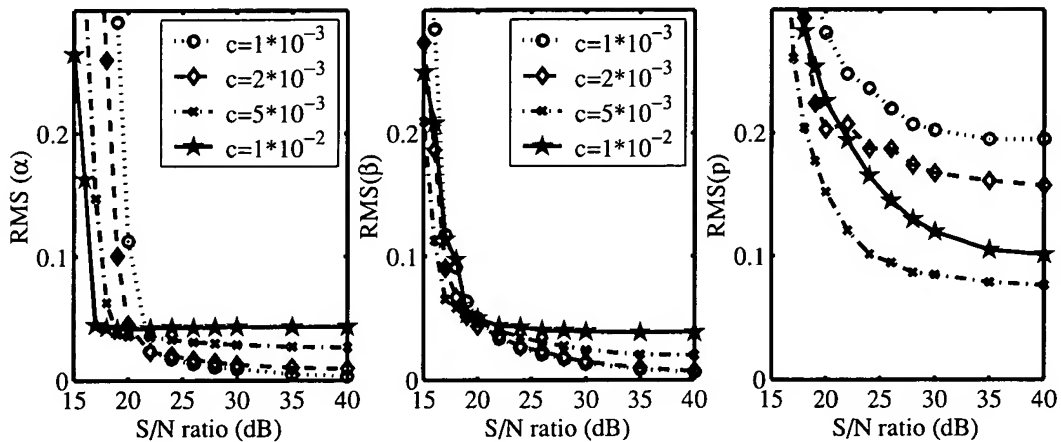


Figure 16. Uncertainty in estimates for α , β and p for different c values as a function of the S/N ratio. The estimated horizontal slowness is compared to the slowness of the direct arrival.

0.02 m thick layers. Synthetic data are computed using a reflectivity method (Kennett 1983). The explosive line source is located at a depth of 100 m and 50 m offset, and emits a 120 Hz Ricker wavelet. The buried geophone is located at a depth of 1.0 m. Fig. 18 shows the synthetic traces for both the surface and buried multicomponent geophones. Data-estimated propagators are shown in Fig. 19. These are compared with theoretical solutions with effective medium velocities, the lower and upper bounds of which are given by the Reuss and Voigt average velocities (Wang & Nur 1992). For the top 1.0 m, the Reuss velocities are $\alpha^- = 259 \text{ m s}^{-1}$ and $\beta^- = 101 \text{ m s}^{-1}$, and the Voigt velocities are $\alpha^+ = 284 \text{ m s}^{-1}$ and $\beta^+ = 105 \text{ m s}^{-1}$ respectively. The average value of the Voigt and Reuss velocities is used to compute the theoretical propagator. Although the propagator waveforms do not exactly match, the time lags of the peaks are similar. Fig. 20 shows cross-sections of the misfit function. Both α and β are well constrained, whereas p cannot be resolved. The estimated velocities are $\alpha = 272 \pm 8 \text{ m s}^{-1}$ and

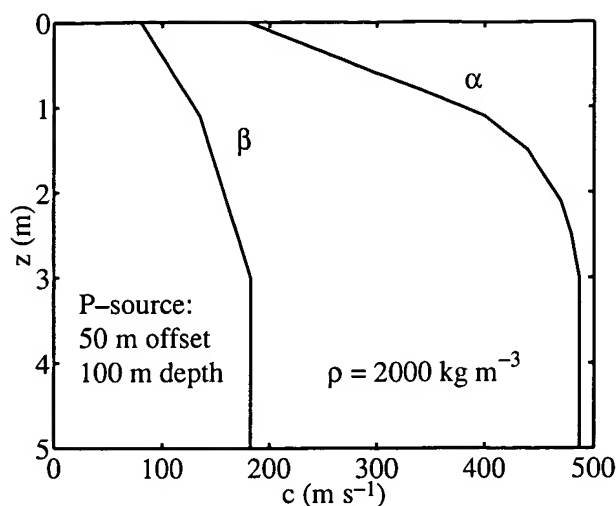


Figure 17. Gradient velocity model and source location.

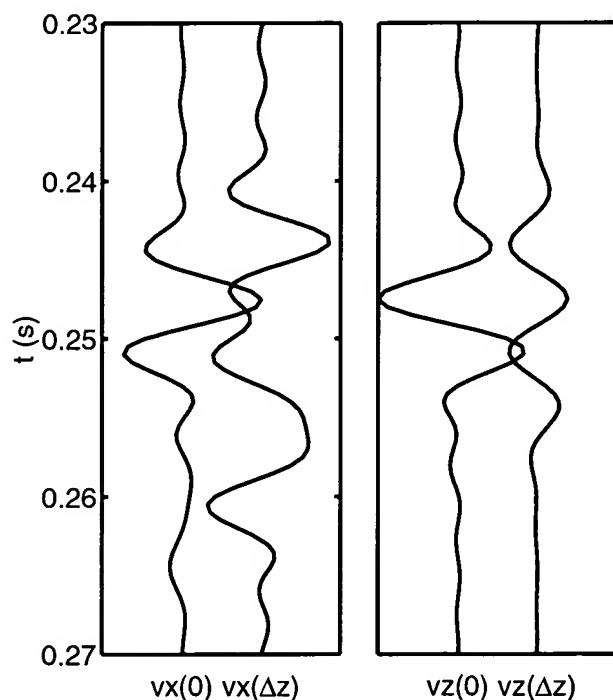


Figure 18. Synthetic data recorded in the gradient model at 50 m offset. The buried geophone is located at a depth of 1.0 m and the P source at a depth of 100 m.

$\beta = 102.8 \pm 0.6 \text{ m s}^{-1}$. These values are obtained by performing repeated experiments ($N = 1000$) with different manifestations of random noise ($S/N = 25 \text{ dB}$), determining the minimum of the objective function E with a forward search method, and using the average and standard deviation of all these estimates. The obtained velocities fall within the Voigt and Reuss bounds for effective medium velocities.

5 DISCUSSION

Three methods to estimate near-surface properties were evaluated in this paper. The first two methods are based on inversion of the wave equation, whereas the third method inverts wavefield propagator filters for near-surface velocities. A fundamental difference between the methods is that wave-equation inversion schemes use amplitude information to constrain α and β . By changing α and β , the amplitudes in the wave equation change, not the phase. On the other hand, propagator inversion uses predominantly phase information to constrain α and β , i.e. the time lags of the peaks in the propagator coefficients are controlled by the wave velocities.

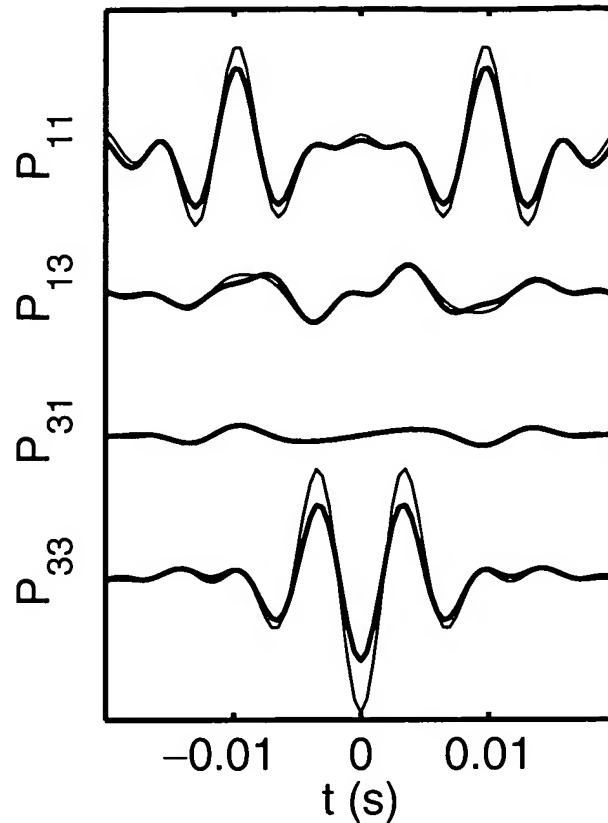


Figure 19. Data-estimated and theoretical propagators in the gradient model. The theoretical propagator is computed using the average value of the Voigt and Reuss effective medium velocities: $\alpha = 272 \text{ m s}^{-1}$ and $\beta = 103 \text{ m s}^{-1}$, $p = 8.75 \times 10^{-4} \text{ (s m}^{-1}\text{)}$ and $c = 10^{-3}$.

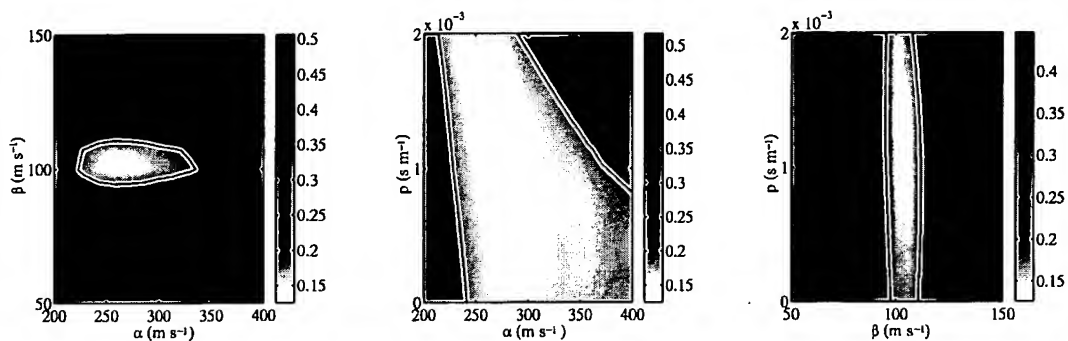


Figure 20. Cross-sections through the minimum of the objective function E for the gradient model. A contour is drawn for $E = 0.20$ and $c = 10^{-3}$.

These sensitivities for either predominantly amplitude information or phase information result in a different optimum experimental set-up. Wave-equation inversion techniques require the measurement of spatial wavefield derivatives, with a spatial geophone spacing on a subwavelength scale. Propagator inversion on the other hand uses mainly phase information. To estimate time differences accurately, both the depth separation of the surface and the buried geophone and the bandwidth of the recorded signal have to be larger. For this reason, we used different configurations, different frequencies and a different depth of the buried geophone, to compare wave-equation inversion techniques with propagator inversion.

Before fitting the waveforms in the wave-equation inversion schemes, either spatial wavefield derivatives or interpolants need to be evaluated. For an accurate implementation of these methods, the spacing between geophones must be sufficiently close, approximately $1/6$ of the effective wavelength. Since the wavelength depends on the material properties, some prior knowledge has to be available to design the receiver group.

Propagator inversion on the other hand has no wavelength constraints on the maximum allowed separation of geophones. Therefore, the method may be applicable to borehole recordings. This has been demonstrated for the SH case by Trampert *et al.* (1993). However, in

the P - SV case we only treated the elastic situation, whereas attenuation has to be included in the formulation for borehole applications. The near-surface velocity estimates presented in this paper are not affected by attenuation, because the geophone separation $\Delta z \ll \lambda$.

However, for a geophone buried at too shallow a depth, propagator inversion cannot resolve the wave velocities. Then, small errors in the phase will cause large uncertainties in the estimated velocities, especially for α . These uncertainties are reduced by increasing the depth of the buried geophone (Van den Berg *et al.* 2003). The minimum depth for the buried geophone depends on the frequency band, the angle of incidence, on α and on the time sampling rate.

The wave-equation inversion schemes use the complete wavefield as input signal. Any event which satisfies the wave equation provides constraints on the near-surface properties. The main sources of error which need to be dealt with are deployment-related errors. Muijs *et al.* (2002) demonstrated that errors such as misorientation and mislocation of individual geophones significantly affect estimates of spatial wavefield derivatives. Correction schemes need to be developed to compensate for these effects. Propagator inversion, on the other hand, avoids the explicit computation of spatial wavefield derivatives. As a consequence, this method is less sensitive to these types of errors.

In contrast to wave-equation inversion techniques, a single slowness assumption is required to construct and invert the propagator filters. As a consequence, those data containing arrivals that are isolated in time need to be selected before this method can be applied. We demonstrated, however, that in a medium with a near-surface low-velocity layer, estimates for α and β are not significantly affected by signal-generated reverberations, and that in a model with a strong velocity gradient, effective medium parameters are obtained.

The following strategies for propagator inversion can be developed by combining data of different shots. First, if the horizontal slownesses in selected data show little variation for different shot points it is possible to reduce effects of noise by stacking the estimated propagator filters. Second, propagator inversion can be formulated without requiring the isolation of an event which can be approximated by a single plane wave. When using a dense source array, the frequency–wavenumber spectra can be computed for common receiver gathers of both the surface geophone and the geophone at depth. Consequently, propagator filters can be determined for each wavenumber or horizontal slowness individually by a spectral division of these two spectra. Thus, propagator inversion is potentially applicable to the complete wavefield. However, difficulties might arise due to lateral variations in near-surface material parameters and poor repeatability of the source.

Synthetic tests have been performed in two dimensions, whereas 3-D wave propagation has to be considered in the field. Applications in the field require a different acquisition geometry for wave-equation inversion. Wave-equation inversion techniques require a 2-D patch of 4×4 receivers at the surface and a buried geophone in the centre at this geophone group. Then, all spatial and temporal derivatives or interpolants can be computed. Propagator inversion requires the separation of P - SV waves from SH waves, hence rotation of the recordings in the in-line/cross-line direction is required. Furthermore, propagator inversion is aided by an estimate for the horizontal slowness in the in-line direction, and therefore a cross pattern of receivers at the surface is recommended for field applications. The general characteristics of the considered methods do not change in three dimensions, and therefore the presented 2-D synthetic results will apply to the 3-D situation.

6 CONCLUSIONS

We evaluated three methods for estimating local near-receiver material properties. A fundamental difference between the methods is that the wave-equation inversion schemes constrain the P -wave and S -wave velocities by matching amplitudes in the wave equation, whereas propagator inversion constrains the wave velocities using predominantly phase information, i.e. with the traveltimes from the free surface to the depth of the buried geophone. As a consequence, wave-equation and propagator inversion have different optimum receiver configurations. For wave-equation inversion, the configuration needs to be designed to allow the measurement of spatial wavefield derivatives or interpolants, whereas the configuration in propagator inversion must allow a reliable measurement of a phase difference.

Both the derivative and the integral formulation for wave-equation inversion are almost equally sensitive to the effects of measurement errors. If a configuration with more than one buried geophone would have been allowed, an interpolation scheme may be developed which is less sensitive to these type of errors. However, these configurations are not convenient for practical applications, and therefore were not considered.

Propagator inversion has two advantages and one disadvantage over wave-equation inversion schemes. First, instead of a 3-D receiver configuration, only two geophones are required, one positioned at the surface and one buried. Second, this scheme avoids the explicit evaluation of spatial wavefield derivatives or interpolants and therefore it is less sensitive to deployment-related errors. On the other hand, this technique implicitly assumes that a data window containing arrivals with a similar horizontal slowness can be isolated in the recorded data, whereas wave-equation inversion schemes are applicable to nearly complete recordings. Synthetic experiments were performed to assess the consequences of the single slowness assumption in propagator inversion. These experiments demonstrated that the method is robust with respect to signal-generated reverberations, and in the case of a near-surface velocity gradient, results are consistent with effective medium velocities, the upper and lower bounds of which are given by the Voigt and Reuss averaged velocities. Moreover, when using a shot array, propagator inversion could be formulated without the plane wave assumption, and therefore it is potentially applicable to the complete wavefield.

ACKNOWLEDGMENTS

We thank Remco Muijs and Dirk-Jan van Manen for discussions and suggestions, and D. J. Verschuur and an anonymous reviewer for their constructive comments.

REFERENCES

- Aki, K. & Richards, P.G., 2002. *Quantitative Seismology*, 2nd edn, University Science Books, Sausalito, CA, USA.
- Aritman, B.C., 2001. Repeatability study of seismic source signatures, *Geophysics*, **66**, 1811–1817.
- Bachrach, R., Dvorkin, J. & Nur, A.M., 2000. Seismic velocities and Poisson's ratio of shallow unconsolidated sands, *Geophysics*, **65**, 559–564.
- Ben-Menahem, A. & Singh, S.J., 1981. *Seismic Waves and Sources*, Dover, New York.
- Curtis, A. & Robertsson, J.O.A., 2002. Volumetric wavefield recording and wave-equation inversion for near-surface material properties, *Geophysics*, **67**, 1602–1611.
- Dankbaar, J.W.M., 1985. Separation of P- and S-waves, *Geophys. Prospect.*, **33**, 970–986.
- de Hoop, A.T. & van der Hijden, J.H.M.T., 1983. Generation of acoustic waves by an impulsive line source in a fluid/solid configuration with a plane boundary, *J. acoust. Soc. Am.*, **74**, 333–342.
- Gao, L., Parker, K.J., Lerner, R.M. & Levinson, S.F., 1996. Imaging of the elastic properties of tissue—a review, *Ultrasound Med. Biol.*, **22**, 959–977.
- Goupillaud, P.L., 1961. An approach to inverse filtering of near-surface layer effects from seismic records, *Geophysics*, **26**, 754–760.
- Helmberger, D. & Wiggins, R.A., 1971. Upper mantle structure of Midwestern United States, *J. geophys. Res.*, **76**, 3229–3245.
- Kähler, S. & Meissner, R., 1983. Radiation and receiver pattern of shear and compressional waves as a function of Poisson ratio, *Geophys. Prospect.*, **31**, 421–435.
- Kennett, B.L.N., 1983. *Seismic Wave Propagation in Stratified Media*, Cambridge University Press, Cambridge.
- Langston, C.A., 1979. Structure under Mount Rainier, Washington, inferred from teleseismic body waves, *J. geophys. Res.*, **84**, 4749–4762.
- Levander, A.R., 1988. Fourth-order finite-difference P–SV seismograms, *Geophysics*, **53**, 1425–1435.
- Mindlin, R.D., 1949. Compliance of elastic bodies in contact, *J. Appl. Mech.*, **16**, 259–268.
- Muijs, R., Holliger, K. & Robertsson, J.O.A., 2002. Perturbation analysis of an explicit wavefield separation scheme for P- and S-waves, *Geophysics*, **67**, 1972–1982.
- Muthupillai, R., Lomas, D.J., Rossman, P.J., Greenleaf, J.F., Manduca, A. & Ehman, R.L., 1995. Magnetic resonance elastography by direct visualization of propagating acoustic strain waves, *Science*, **269**, 1854–1857.
- Oliphant, T., Mahowald, J.L., Ehman, R.L. & Greenleaf, J.F., 1999. Complex-valued quantitative stiffness estimation using dynamic displacement measurements and local inversion of conservation of momentum, *IEEE Ultrasonics Symp.*, Vol. 2, 1641–1644.
- Oliphant, T.E., Manduca, A., Ehman, R.L. & Greenleaf, J.F., 2001. Complex-valued stiffness reconstruction for magnetic resonance elastography by algebraic inversion of the differential equation, *Magn. Reson. Med.*, **45**, 299–310.
- Osen, A., Amundsen, L. & Reitan, A., 1999. Removal of water-layer multiples from multicomponent sea-bottom data, *Geophysics*, **64**, 838–851.
- Robertsson, J.O.A. & Muyzert, E., 1999. Wavefield separation using a volume distribution of three component recordings, *Geophys. Res. Lett.*, **26**, 2821–2824.
- Romano, A., Bucaro, J.A., Ehman, R.L. & Shirron, J.J., 2000. Evaluation of a material parameter extraction algorithm using MRI-based displacement measurements, *IEEE Trans. Ultrason. Ferroelectr. Freq. Control*, **47**, 1575–1581.
- Romano, A.J., Shirron, J.J. & Bucaro, J.A., 1998. On the noninvasive determination of material parameters from a knowledge of elastic displacements: theory and numerical simulation, *IEEE Trans. Ultrason. Ferroelectr. Freq. Control*, **45**, 751–759.
- Toksöz, M.N., Cheng, C.H. & Timur, A., 1976. Velocities of seismic waves in porous rocks, *Geophysics*, **41**, 621–645.
- Trampert, J., Cara, M. & Frogneux, M., 1993. SH propagator matrix and Q_s estimates from borehole- and surface- recorded earthquake data, *Geophys. J. Int.*, **112**, 290–299.
- Unser, M., 1999. Splines, a perfect fit for signal and image processing, *IEEE Signal Process. Mag.*, **16**(6), 22–38.
- Van den Berg, J., Curtis, A. & Trampert, J., 2003. Optimal nonlinear Bayesian experimental design: an application to amplitude versus offset experiments, *Geophys. J. Int.*, **155**, 411–421.
- Van Houten, E.E.W., Paulsen, K.D., Miga, M.I., Kennedy, F.E. & Weaver, J.B., 1999. An overlapping subzone technique for MR-based elastic property reconstruction, *Magn. Reson. Med.*, **42**, 779–786.
- Wang, Z. & Nur, A., 1992. *Seismic and Acoustic Velocities in Reservoir Rocks, vol. 2, Theoretical and Model Studies*, Geophysics Reprint Series no 10, Society of Exploration Geophysicists, Tulsa, OK, USA.
- Wapenaar, C.P.A., Herrmann, P., Verschuur, D.J. & Berkhout, A.J., 1990. Decomposition of multicomponent seismic data into primary P- and S-wave responses, *Geophys. Prospect.*, **38**, 633–661.

APPENDIX A: COEFFICIENTS FOR DIRECT WAVE-EQUATION INVERSION

The measurable coefficients in eqs (6)–(8) for direct wave-equation inversion are found by inserting the free-surface derivative conditions, eqs (3)–(5), into the wave eq. (1):

$$A_1(t) = \frac{2}{\Delta z}(\partial_1 v_3 + \partial_3 v_1) + \nabla_H^2 v_1 + 2\partial_1(\nabla_H \cdot \mathbf{v}_H), \quad (\text{A1})$$

$$A_2(t) = \frac{2}{\Delta z}(\partial_2 v_3 + \partial_3 v_2) + \nabla_H^2 v_2 + 2\partial_2(\nabla_H \cdot \mathbf{v}_H), \quad (\text{A2})$$

$$A_3(t) = \frac{2}{\Delta z}(\nabla_H \cdot \mathbf{v}_H + \partial_3 v_3) - \nabla_H^2 v_3, \quad (\text{A3})$$

$$B_1(t) = 2\partial_1(\nabla_H \cdot \mathbf{v}_H), \quad (\text{A4})$$

$$B_2(t) = 2\partial_2(\nabla_H \cdot \mathbf{v}_H), \quad (\text{A5})$$

and

$$B_3(t) = \frac{4}{\Delta z}(\nabla_H \cdot \mathbf{v}_H) - 2(\nabla_H^2 v_3). \quad (\text{A6})$$

The finite-difference (FD) first-order derivatives in depth are denoted $\partial_3 v$ and are given by:

$$\partial_3 v(\Delta z/2) = \frac{v(\Delta z) - v(0)}{\Delta z} + O(\Delta z^2), \quad (\text{A7})$$

with Δz the depth beneath the free surface of the buried geophone. The vertical derivative cannot be measured exactly at the free surface but at depth $\Delta z/2$. The following notation is used for horizontal wavefield derivatives:

$$\nabla_H = [\partial_1 \quad \partial_2]^T, \quad (A8)$$

and

$$\mathbf{v}_H = [v_1 \quad v_2]^T \quad (A9)$$

Temporal and spatial wavefield derivatives are computed using finite-difference operators.

APPENDIX B: INTEGRAL EQUATION FORMULATION

We demonstrate that the wave eq. (1) can be transformed into an integral equation. Let $\mathbf{w} = (w_1, w_2, w_3)^T$ be a sufficient smooth vector-valued function and Ω a volume bounded by a surface Γ . If the wave equation is multiplied by \mathbf{w} and integrated over the volume Ω , the result is:

$$\int_{\Omega} \mathbf{w} \cdot \ddot{\mathbf{v}} d\Omega = \int_{\Omega} \mathbf{w} \cdot [\alpha^2 \nabla(\nabla \cdot \mathbf{v}) - \beta^2 \nabla \times (\nabla \times \mathbf{v})] d\Omega. \quad (B1)$$

The first term of the right-hand side of eq. (B1) can be expanded by repeated application of the divergence theorem:

$$\begin{aligned} \int_{\Omega} d\Omega \mathbf{w} \cdot [\nabla(\nabla \cdot \mathbf{v})] &= \int_{\Gamma} d\Gamma [\mathbf{w}(\nabla \cdot \mathbf{v})] \cdot \mathbf{n} - \int_{\Omega} d\Omega (\nabla \cdot \mathbf{w})(\nabla \cdot \mathbf{v}) \\ &= \int_{\Gamma} d\Gamma [\mathbf{w}(\nabla \cdot \mathbf{v}) - \mathbf{v}(\nabla \cdot \mathbf{w})] \cdot \mathbf{n} + \int_{\Omega} d\Omega \mathbf{v} \cdot [\nabla(\nabla \cdot \mathbf{w})], \end{aligned} \quad (B2)$$

where \mathbf{n} is the outward-pointing normal vector on Γ . The second term is expanded using the identity,

$$\nabla \times (\nabla \times \mathbf{v}) = \nabla(\nabla \cdot \mathbf{v}) - \nabla^2 \mathbf{v} \quad (B3)$$

and the divergence theorem:

$$\begin{aligned} \int_{\Omega} d\Omega \mathbf{w} \cdot [\nabla \times (\nabla \times \mathbf{v})] &= \int_{\Gamma} d\Gamma [\mathbf{w}(\nabla \cdot \mathbf{v}) - \mathbf{v}(\nabla \cdot \mathbf{w}) - \mathbf{w} \cdot (\nabla \mathbf{v})^T + \mathbf{v} \cdot (\nabla \mathbf{w})^T] \cdot \mathbf{n} \\ &\quad + \int_{\Omega} d\Omega \mathbf{v} \cdot [\nabla \times (\nabla \times \mathbf{w})] d\Omega. \end{aligned} \quad (B4)$$

In the volume integrals, all spatial wavefield derivatives have disappeared in eq. (B4). Because the vector-valued functions \mathbf{w} can be chosen arbitrarily, boundary conditions can be imposed such that the surface integrals vanish. Consequently, all spatial wavefield derivatives can be made to disappear.